Cell Stem Cell

Article

Organoid modeling of Zika and herpes simplex virus 1 infections reveals virus-specific responses leading to microcephaly

Graphical abstract

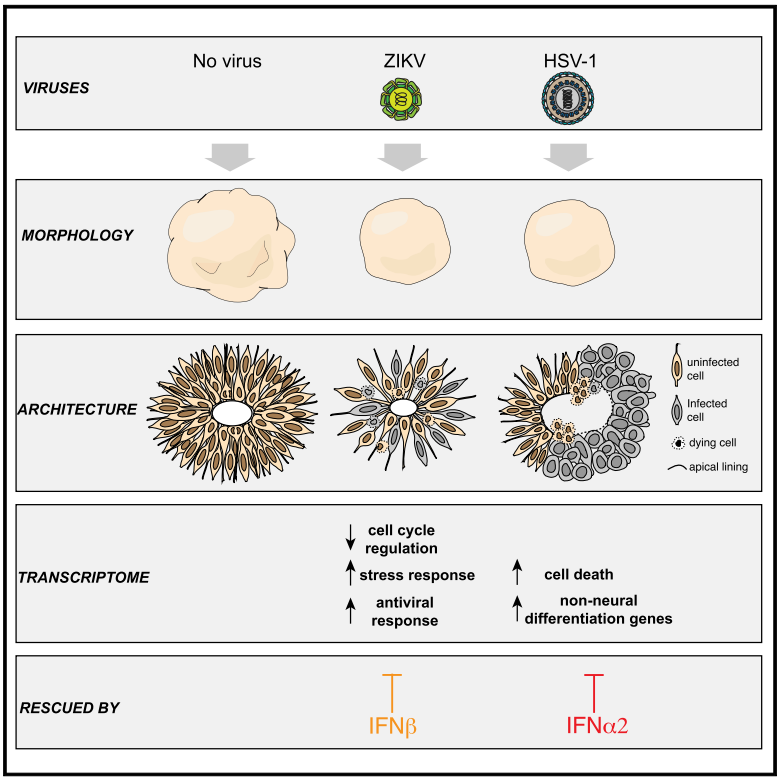

Highlights

- ZIKV and HSV-1 impair brain organoid growth
- ZIKV and HSV-1 induce distinct morphological defects and transcriptional signatures
- The two viruses differentially engage the interferon system
- ZIKV and HSV-1-induced defects can be rescued by distinct interferons

Authors

Veronica Krenn, Camilla Bosone, Thomas R. Burkard, ..., Patricia Pestana Garcez, Ali Mirazimi, Jürgen A. Knoblich

Correspondence

juergen.knoblich@imba.oeaw.ac.at

In brief

Krenn et al. used human brain organoids to compare the effects of ZIKV and HSV-1 on brain development. They reveal that the two viruses impair organoid growth by inducing distinct morphological and transcriptional changes. Moreover, the specific defects caused by ZIKV and HSV-1 can be prevented by distinct interferons.

Krenn et al., 2021, Cell Stem Cell *28*, 1–18
August 5, 2021
https://doi.org/10.1016/j.stem.2021.03.004

CellPress

Cell Stem Cell

CellPress

Article

Organoid modeling of Zika and herpes simplex virus 1 infections reveals virus-specific responses leading to microcephaly

Veronica Krenn,[1] Camilla Bosone,[1] Thomas R. Burkard,[1] Julia Spanier,[2] Ulrich Kalinke,[2,3] Arianna Calistri,[4] Cristiano Salata,[4] Raissa Rilo Christoff,[5] Patricia Pestana Garcez,[5] Ali Mirazimi,[6,7] and Jürgen A. Knoblich[1,8,9,*]

[1]Institute of Molecular Biotechnology (IMBA), Austrian Academy of Sciences, Vienna BioCenter (VBC), Vienna 1030, Austria
[2]Institute for Experimental Infection Research, TWINCORE, Centre for Experimental and Clinical Infection Research, a Joint Venture between the Helmholtz Centre for Infection Research, Braunschweig, and the Hanover Medical School, Hanover 30625, Germany
[3]Cluster of Excellence – Resolving Infection Susceptibility (RESIST), Hanover Medical School, Hanover 30625, Germany
[4]Department of Molecular Medicine, University of Padua, Padua 35121, Italy
[5]Institute of Biomedical Sciences, Federal University of Rio de Janeiro, Rio de Janeiro 21941-901, Brazil
[6]Department of Laboratory Medicine (LABMED), Karolinska Institute, Stockholm 17177, Sweden
[7]National Veterinary Institute, Uppsala 75189, Sweden
[8]Medical University of Vienna, Vienna 1030, Austria
[9]Lead contact
*Correspondence: juergen.knoblich@imba.oeaw.ac.at
https://doi.org/10.1016/j.stem.2021.03.004

SUMMARY

Viral infection in early pregnancy is a major cause of microcephaly. However, how distinct viruses impair human brain development remains poorly understood. Here we use human brain organoids to study the mechanisms underlying microcephaly caused by Zika virus (ZIKV) and herpes simplex virus (HSV-1). We find that both viruses efficiently replicate in brain organoids and attenuate their growth by causing cell death. However, transcriptional profiling reveals that ZIKV and HSV-1 elicit distinct cellular responses and that HSV-1 uniquely impairs neuroepithelial identity. Furthermore, we demonstrate that, although both viruses fail to potently induce the type I interferon system, the organoid defects caused by their infection can be rescued by distinct type I interferons. These phenotypes are not seen in 2D cultures, highlighting the superiority of brain organoids in modeling viral infections. These results uncover virus-specific mechanisms and complex cellular immune defenses associated with virus-induced microcephaly.

INTRODUCTION

Viral infection during pregnancy is a major cause of fetal brain malformation. Transmission of infectious agents from mother to fetus can be devastating for fetal brain development (Bale and Murph, 1992; Brasil et al., 2016; Marquez et al., 2011). Infections account for up to 50% of cases of congenital microcephaly (Herber et al., 2019; Mlakar et al., 2016), and those occurring in the first trimester of pregnancy are typically associated with more severe outcomes (Coyne and Lazear, 2016). Despite these overlapping phenotypes, congenital infections are caused by distinct pathogens collectively referred to as TORCH (*Toxoplasma* gondii, other, *Rubella*, human cytomegalovirus [HCMV], herpes simplex viruses 1 and 2 [HSV-1 and HSV-2, respectively], and Zika virus [ZIKV]) (Schwartz, 2017). HCMV and HSV infections are the most common causes of newborn morbidity worldwide (Looker et al., 2017; Marsico and Kimberlin, 2017) and the newly emerged ZIKV remains a threat for pregnant women (Anderson and Humphreys, 2019).

However, whether TORCH pathogens alter fetal brain development via similar mechanisms is unclear. Mechanistic understanding has been hampered by the lack of accurate models for individual TORCH infections. Although rodents can, in part, reproduce microcephaly caused by ZIKV and CMV (Li et al., 2016; Li and Tsutsui, 2000), they are not the natural hosts and do not faithfully recapitulate TORCH neuropathology (Cheeran et al., 2009; Ming et al., 2016). Human brain organoid systems derived from human pluripotent stem cells (hPSCs) are emerging as human three-dimensional (3D) culture platforms for the study of viral infections and their effect on human neurodevelopment (Kim et al., 2019). Brain organoids recapitulate the cell composition and 3D environment of the embryonic human brain (Di Lullo and Kriegstein, 2017; Lancaster et al., 2013), overcoming a major limitation of human two-dimensional (2D) culture systems (Baker and Chen, 2012; Duval et al., 2017). Organoid models are used widely to recapitulate the structural defects, cell depletion, and molecular signatures associated with ZIKV-induced microcephaly (Cugola et al., 2016; Gabriel et al., 2017; Garcez et al., 2016; Qian et al., 2016; Watanabe et al., 2017) as well as to model part of the neuropathological defects caused by HCMV and HSV-1 (Brown et al., 2019; Qiao et al., 2020; Sison et al.,

2019; Sun et al., 2020). However, a comparative analysis of organoid models of TORCH-induced microcephaly is lacking.

One potential common underlying mechanisms of TORCH-induced microcephaly is the activation of the innate immune response and its detrimental effects on fetal brain development (Gottfried et al., 2015; Watanabe et al., 2010). In particular, activation of cytokines called type I interferons (IFN-I), which include several α species (IFNα) and one β species (IFNβ), upon infection is required to induce an array of antiviral effectors referred to as IFN-stimulated genes (ISGs) that can restrict viral spreading but also promote cell death (Schneider et al., 2014). Several studies using human 2D and 3D neural cultures have reported upregulation of IFN-I, ISGs and immune signatures in response to ZIKV infection (Dang et al., 2016; Ferraris et al., 2019; Hanners et al., 2016; Li et al., 2017; Lima et al., 2019; Liu et al., 2019; Simonin et al., 2016; Watanabe et al., 2017; Zhang et al., 2016). However, the magnitude of this response varies substantially across studies. Furthermore, the function of this response in the pathogenesis of ZIKV infection remains debated; evidence supporting a neuroprotective function of IFN-I (Li et al., 2017; Lin et al., 2019) and a detrimental neuroinflammatory effect (Dang et al., 2016; Liu et al., 2019) exist. Although these discrepancies are in part due to changes in cell differentiation stages and viral strains (Ferraris et al., 2019; Simonin et al., 2016), whether differences between 2D versus 3D culture systems and/or changes in cell type composition contribute to the magnitude and function of the innate immune response remains unclear. Finally, little is known about activation of the antiviral response in other human models of TORCH-induced microcephaly; thus, a unifying view of the role of the innate immune response is missing.

Here we used human brain organoids to reproduce the microcephaly-like phenotype caused by multiple TORCH viruses, including ZIKV, HCMV, and HSV-1, which differ in their viral genome structure, size, and mode of replication (Table S1). We show that these organoid models exhibit major differences in their structure, transcriptional profiles, engagement of the IFN-I system, and sensitivity to IFN-I. These results argue for the existence of unique pathogenic mechanisms and a neuroprotective role of IFN-I responses underlying virus-induced microcephaly.

RESULTS

ZIKV and HSV-1 infections impair growth of early-stage brain organoids

To compare the effects of distinct TORCH viruses on the early stages of human brain development, we generated brain organoids using our previously established protocol (Lancaster et al., 2013) and exposed them to a virus inoculum for 24 h. We focused on day 10 organoids, an early organoid stage that expresses the neuroectodermal markers Nestin and Pax6 (Figures S1A and S1B) and is highly susceptible to viral infection (Dang et al., 2016; Gabriel et al., 2017).

We first exposed brain organoids to ZIKV, and, after inoculum removal, organoids were examined 4, 8, and 12 days post infection (dpi). Although mock-treated organoids grew over time, ZIKV-exposed organoids exhibited time-dependent growth attenuation and were significantly smaller at 12 dpi (Figures 1A and 1B; Table S2). Concomitantly, we observed increasing expression of ZIKV viral RNA (vRNA) and the release of infectious ZIKV particles at 4 and 12 dpi (Figures 1C and 1D), indicating productive infection. Staining for the ZIKV antigen (ZIKVA) and the human neural progenitor cell (hNPC) marker Sox1 revealed foci of infection at 4 dpi (Figure 1E), confirming hNPCs as the main cellular targets of ZIKV infection. Because a microcephaly phenotype can be described at the tissue level by a cell depletion phenotype, we analyzed hNPC abundance by measuring the area of ventricular zone (VZ)-like structures where hNPCs reside. At 12 dpi, although mock-treated organoids showed the typical organization of VZ-like regions, ZIKV-infected organoids contained fewer and smaller VZ-like structures (Figures 1F and 1G). Furthermore, analysis of apoptosis at 12 dpi by staining for the apoptotic marker cleaved caspase-3 (CC3) showed an increase in ZIKV-infected cultures in ZIKVA-positive and -negative cells (Figures S1C–S1E). Because hNPC depletion can result in lumen size changes, we also measured the lumen area and found it to be reduced in ZIKV-infected organoids (Figure S1F). These findings are in line with the ability of ZIKV to attenuate organoid growth and cause hNPC depletion (Cugola et al., 2016; Gabriel et al., 2017; Garcez et al., 2016; Qian et al., 2016; Watanabe et al., 2017) and, thus, validate our infection paradigm for the study of virus-induced microcephaly.

To examine the effects of other TORCH viruses, we exposed organoids to a strain of HCMV expressing the mNeonGreen fluorescent reporter (HCMV-mNG; Kasmapour et al., 2017) and to another herpesvirus, HSV-1. We observed mNG fluorescence in HCMV-exposed organoids at 4 dpi and in a minority of Sox1+ cells after immunostaining (Figures S1G–S1I). However, HCMV infection remained limited to small clusters of cells at 12 dpi and did not attenuate organoid growth (Figures S1G–S1K). These observations indicate that HCMV does not replicate efficiently and does not cause a microcephaly-like phenotype in early-stage organoids. In contrast to this, organoids exposed to HSV-1 disintegrated at 8 dpi (Figures S1L and S1M), uncovering the destructive nature of HSV-1 infection. Organoids exposed to a lower dose of HSV-1 still showed impaired growth at 8 dpi (Figures 1H and 1I; Table S2) but preserved tissue integrity to a certain extent. We observed productive HSV-1 infection at this lower dose, as evidenced by time-dependent expression of the HSV-1 thymidine kinase (TK) gene and production of infectious HSV-1 particles (Figures 1J and 1K). Because TK expression at 4 dpi was low and variable, HSV-1 tropism at 4 dpi was analyzed in organoids exposed to the higher HSV-1 dose. This revealed infection of Sox1+ hNPCs and the typical chromatin marginalization to the nuclear periphery caused by HSV-1 replication (Aho et al., 2017; Figures 1L and 1M). Immunostaining of tissues infected with a low HSV-1 dose revealed disrupted cytoarchitecture characterized by fewer and smaller VZ-like regions at 8 dpi (Figures 1N and 1O). Moreover, analysis of the fraction of apoptotic cells at 8 dpi showed an increase in HSV-1-infected cultures and their accumulation in the lumen (Figures S1N and S1O). Unlike ZIKV, lumens of HSV-1-infected organoids appeared to be enlarged (Figure S1P), likely as a result of accumulation of apoptotic cells. Most apoptotic cells (92%) were negative for expression of the immediate-early viral protein ICP4 (Figures S1Q and S1R), suggesting induction of apoptosis in bystander cells and/or abortively infected cells (Drayman et al., 2019). These results indicate that ZIKV and HSV-1, but not HCMV, efficiently infect early-stage brain organoids and

Please cite this article in press as: Krenn et al., Organoid modeling of Zika and herpes simplex virus 1 infections reveals virus-specific responses leading to microcephaly, Cell Stem Cell (2021), https://doi.org/10.1016/j.stem.2021.03.004

CellPress

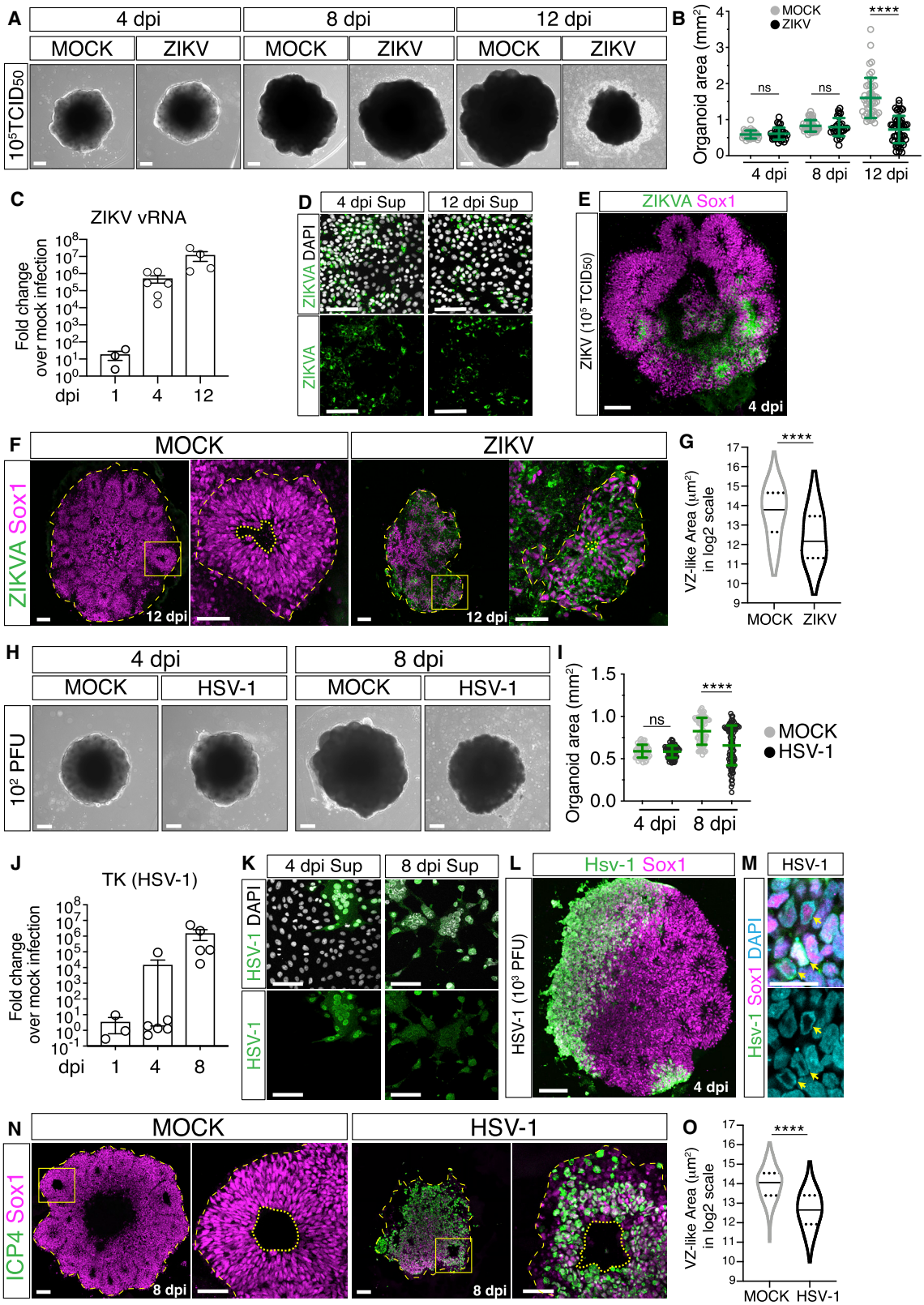

Figure 1. ZIKV and HSV-1 infections impair organoid growth

(A and B) Images (scale bars, 200 µm) and area measurements of organoids exposed to ZIKV or mock treated. Values are mean ± SD and represent individual organoids ($p = 0.7886$, 4 dpi; $p = 0.3190$, 8 dpi; ****$p < 0.0001$; Mann-Whitney test). $TCID_{50}$, mean tissue culture infectious dose.

(legend continued on next page)

Please cite this article in press as: Krenn et al., Organoid modeling of Zika and herpes simplex virus 1 infections reveals virus-specific responses leading to microcephaly, Cell Stem Cell (2021), https://doi.org/10.1016/j.stem.2021.03.004

reduce their growth, mimicking ZIKV- and HSV-1-associated microcephaly.

ZIKV and HSV-1 infections elicit different transcriptional signatures

To investigate the molecular signatures underlying the different organoid growth defects, we analyzed the transcriptional profiles of ZIKV- and HSV-1-infected cultures by RNA sequencing. We confirmed high expression of neural progenitor genes in these datasets (Figure S2A) and focused on transcriptional changes at late time points because very few genes were deregulated at 4 dpi (Figures 2A and 2B), an early infection stage that is not associated with major structural defects (Figure 1). We identified 531 and 423 differentially expressed genes (DEGs) in ZIKV- and HSV-1-infected cultures compared with their mock counterparts. Many DEGs in ZIKV-infected cultures were downregulated and involved in cell cycle and cell division (Figure 2C), whereas almost all DEGs found in HSV-1-infected cultures were upregulated (Figure 2B). Overlap between the two datasets was limited, as only 4.6% of DEGs were shared (Figure 2D).

Gene Ontology (GO) term analysis of genes upregulated in ZIKV-infected cultures revealed enrichment for antiviral defense pathways and response to IFN, stress, or stimuli (Figure 2E). Furthermore, promoters of upregulated genes were enriched in binding sites for transcription factors involved in immune responses (IRF7/9 and STAT1/2) and in the unfolded protein response (UPR; *DDIT3* and *ATF3*) (Figure 2F). Genes implicated in antiviral defense (Schneider et al., 2014) and the UPR were among the most upregulated at 12 dpi (Figure 2G; Table S3), and some were found to be upregulated already at 4 dpi (Figure S2B), confirming activation of immune- and stress-related signatures in ZIKV-infected cultures. In contrast, GO term analysis of HSV-1-infected signatures revealed enrichment in regulation of developmental and cellular processes as well as cell death-related pathways (Figure 2H). Promoters of HSV-1-upregulated genes were enriched in binding sites of key regulators of proliferation, differentiation, apoptosis, and transformation, including members of the transcription factor complex AP-1 (*FOS*, *FOSB*, *JUN*, and *JUNB*) (Hess et al., 2004), *NR4A3* and *NFIL3* (Herring et al., 2019; Keniry et al., 2014), the neural crest regulator *CSRNP1* (Simões-Costa and Bronner, 2015), the epithelial-mesenchymal transition (EMT) inducer *SNAI1* (Carver et al., 2001), and stress response genes (*DDIT3* and *ATF3*) (Figure 2I). Consistent with this, regulators of cell proliferation, apoptosis, and stress response were upregulated in HSV-1-infected cultures (Figure 2J; Table S3). The most upregulated genes also included genes implicated in neural, neural crest, and mesenchymal development and key regulators of lymphocyte and erythrocyte function (Figure 2J; Table S3). We confirmed increased expression of the EMT regulator Snai1 in HSV-1-infected cultures by immunostaining (Figure S2C). These results point to the activation of multiple non-neural pathways in HSV-1-infected cultures.

We hypothesized that this could compromise the neural identity of brain organoids. Thus, we examined neuroepithelial polarity in infected organoids by immunostaining for N-cadherin, which is typically enriched at the apical side in cells surrounding the lumen in mock-treated organoids (Figures 2K and 2L; Kadowaki et al., 2007). Strikingly, N-cadherin accumulation was lost in HSV-1-infected cultures but not in ZIKV-infected organoids (Figures 2K and 2L). Apical accumulation of N-cadherin was reduced in HSV-1-infected hNPCs (Figure 2M), suggesting a cell-autonomous effect. Loss of N-cadherin mainly reflected changes in its localization or protein expression because its mRNA abundance was not reduced severely in infected organoids (Figure S2D). Furthermore, we observed decreased Sox1 protein intensity in HSV-1-infected organoids (Figure S2E), confirming impaired hNPC identity. We also observed similar defects in later-stage organoids infected with HSV-1 (Figures S2F–S2N), demonstrating the ability of HSV-1 to alter differentiation in more fate-restricted cells. These results indicate that HSV-1 specifically activates alternative non-neural developmental programs and disrupts the neuroepithelial integrity of brain organoids, whereas ZIKV infection triggers antiviral and stress-related signatures but maintains cytoarchitecture.

ZIKV and HSV-1 infections differentially engage the IFN-I system

We next explored the mechanisms underlying the differential engagement of antiviral defense pathways by ZIKV and HSV-1 by examining the upregulated signatures from the RNA sequencing data. Cluster analysis of genes upregulated in ZIKV-infected cultures revealed the presence of a highly connected cluster of genes enriched in the IFN-sensitive responsive element (ISRE) in their promoters (Figures 3A and 3B) and, thus,

(C) qRT-PCR analysis of ZIKV viral RNA (vRNA) in organoids exposed to ZIKV. Values are mean ± SEM ($p = 0.1$, 1 dpi; $p = 0.0022$, 4 dpi; $p = 0.0286$, 12 dpi; Mann-Whitney test over age-matched, mock-treated).

(D) Immunostaining of Vero cells (scale bars, 100 μm) incubated with supernatant (sup) of ZIKV-infected organoids. ZIKVA, ZIKV antigen.

(E–G) Immunostaining (scale bars, 100 μm) of organoids exposed to ZIKV or mock treated. Dashed lines indicate organoid contour based on DAPI signal (data not shown). Insets in (F) (scale bars, 50 μm) show a magnified view of the ventricular zone (VZ)-like structures (dashed lines) and their lumens (dotted lines). Violin plots indicate median and quartiles (n = 129 regions from 11 mock-treated, n = 109 from 13 ZIKV organoids from 3 experiments; ****$p < 0.0001$; Mann-Whitney test).

(H and I) Images (scale bars, 200 μm) and area measurements of organoids exposed to HSV-1 (10^2 plaque-forming units [PFUs]) or mock treated. Values are mean ± SD and represent individual organoids ($p = 0.6625$, 4 dpi; ****$p < 0.0001$; Mann-Whitney test).

(J) qRT-PCR analysis of the HSV-1 gene thymidine kinase (TK) in organoids exposed to HSV-1 (10^2 PFU). Values are mean ± SEM ($p > 0.9999$, 1 dpi; $p = 0.4004$, 4 dpi; $p = 0.0079$, 8 dpi; Mann-Whitney test over age-matched, mock-treated).

(K) Immunostaining of Vero cells (scale bars, 100 μm) incubated with supernatant (sup) from HSV-1-infected organoids (10^2 PFU).

(L and M) Immunostaining (scale bars, 100 μm in L, 20 μm in M) of organoids exposed to HSV-1 (10^3 PFU) and analyzed at 4 dpi. Arrows indicate chromatin localization (marked by DAPI) at the nuclear periphery.

(N and O) Immunostaining (scale bars, 100 μm) of organoids exposed to HSV-1 (10^2 PFU) or mock treated. Dashed lines indicate organoid contour based on DAPI signal (data not shown). Insets (scale bars, 50 μm) show a magnified view of VZ-like structures (dashed lines) around lumens (dotted lines). HSV-1 sample images underwent a 180° rotation. Violin plots indicate median and quartiles (n = 146 regions from 15 mock-treated, n = 69 from 16 HSV organoids from 3 experiments; ****$p < 0.0001$, Mann-Whitney test). ICP4, infected cell polypeptide 4 protein of HSV-1.

ns, non-significant; dpi, days post infection. See also Figure S1 and Tables S1 and S2.

Please cite this article in press as: Krenn et al., Organoid modeling of Zika and herpes simplex virus 1 infections reveals virus-specific responses leading to microcephaly, Cell Stem Cell (2021), https://doi.org/10.1016/j.stem.2021.03.004

CellPress

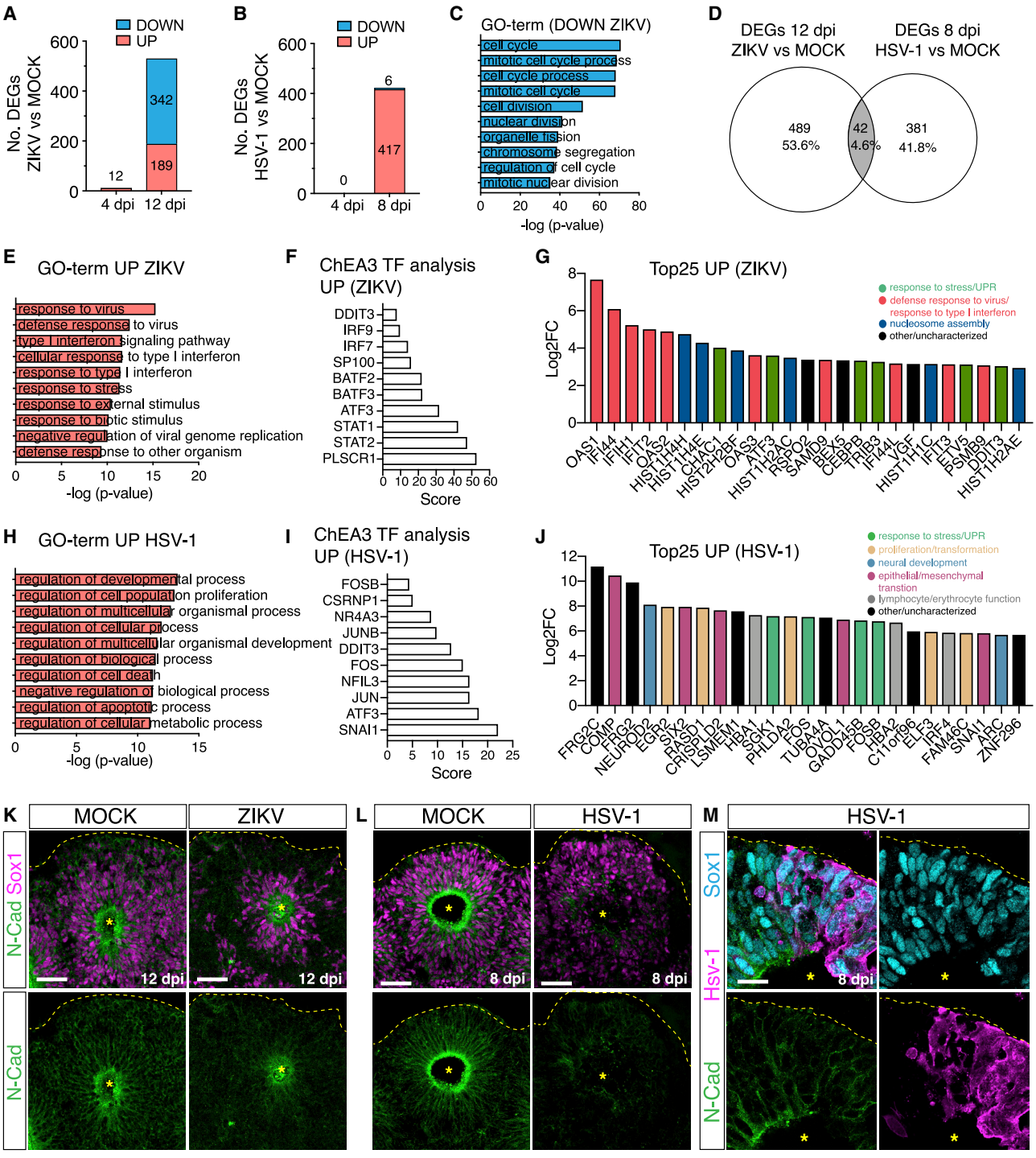

Figure 2. ZIKV and HSV-1 infections elicit distinct transcriptional responses

(A and B) Graphs showing the number of differentially expressed genes (DEGs) in virus-infected organoids.

(C) Top 10 Gene Ontology (GO) terms of downregulated genes (log2 fold change < 1) in ZIKV versus mock-exposed organoids (12 dpi).

(D) Venn diagram showing limited overlap between the two datasets.

(E and H) Top 10 GO terms of upregulated genes (log2 fold change > 2) in virus-infected organoids (12 dpi in E, 8 dpi in H).

(F and I) Top 10 results of ChEA3 transcription factor (TF) analysis performed on upregulated genes.

(G and J) Expression of the top 25 upregulated genes in ZIKV-infected organoids (12 dpi, G) or in HSV-1-infected organoids (8 dpi, J). FC, fold change.

(K–M) Immunostaining (scale bars, 50 μm in K and L, 20 μm in M) of infected and mock-treated organoids. Dashed lines and asterisks indicate organoid surface based on DAPI signal (data not shown) and lumen, respectively.

See also Figure S2 and Table S3.

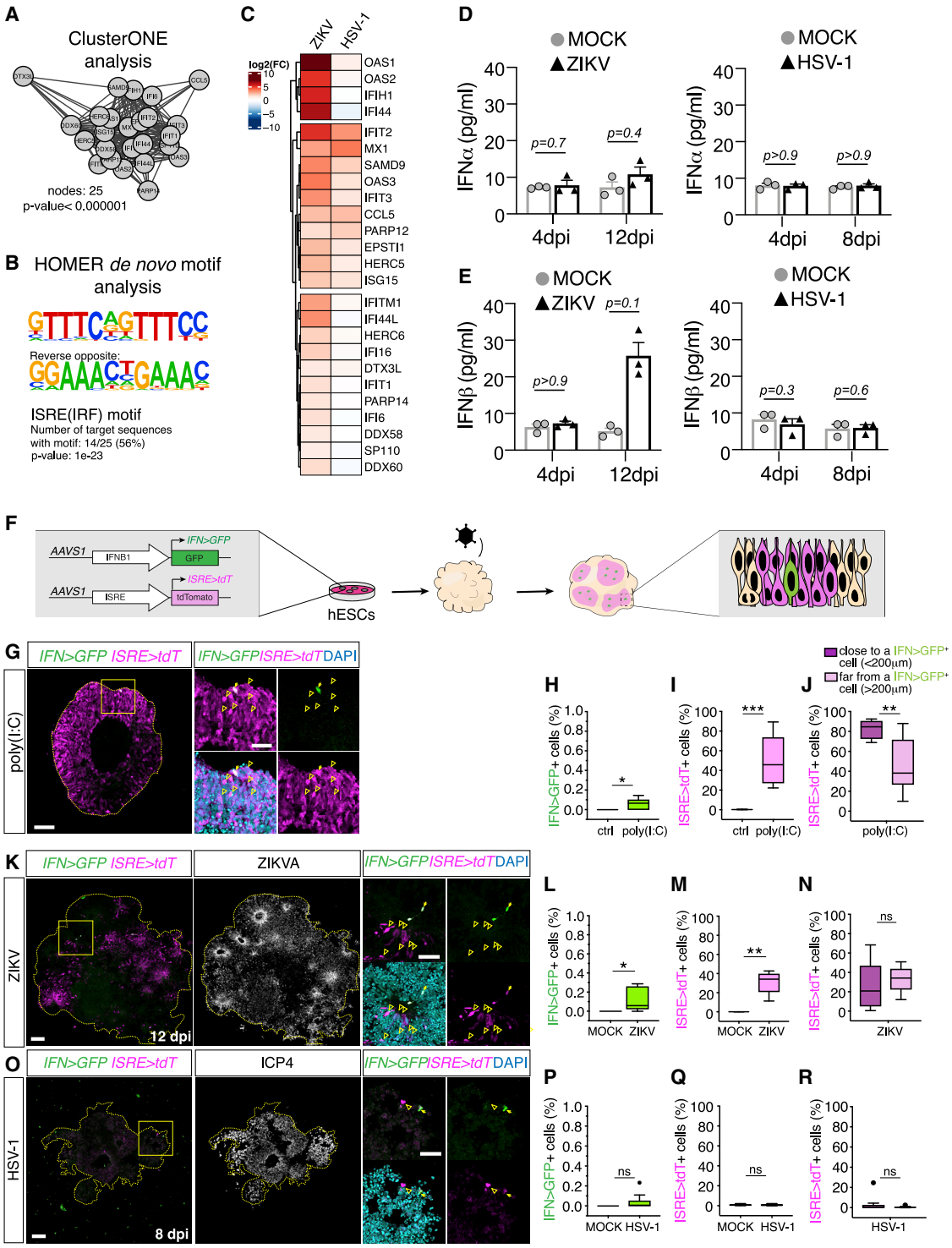

Figure 3. ZIKV and HSV-1 infections differentially engage the IFN-I system

(A and B) Cluster of densely connected genes among genes upregulated in ZIKV-infected organoids at 12 dpi (A) and their HOMER *de novo* motif analysis (B).

(C) Expression analysis of genes from (A) in infected organoids compared with their mock-treated controls.

(D and E) Quantification of IFN *a* and IFNβ levels measured by ELISA. Values represent mean ± SEM (Mann-Whitney test).

(F) Schematic of *IFNB1>GFP* (*IFN>GFP*) and *ISRE>tdTomato* (*ISRE>tdT*) reporters.

(legend continued on next page)

Please cite this article in press as: Krenn et al., Organoid modeling of Zika and herpes simplex virus 1 infections reveals virus-specific responses leading to microcephaly, Cell Stem Cell (2021), https://doi.org/10.1016/j.stem.2021.03.004

mapped to the ISG family (Schneider et al., 2014), in line with a previous study (Liu et al., 2019). Such a signature was not prominent in HSV-1-infected cultures (Figure 3C), and we also confirmed the poor activation of ISGs by HSV-1 at early time points by qRT-PCR analysis (Figures S3A and S3B). Because ISGs are induced potently by IFN-I (Schneider et al., 2014), we measured production of all IFNα species and IFNβ in supernatants from ZIKV and HSV-1-infected organoids by ELISA. We detected a modest (but non-significant) increase in IFNβ specifically in the supernatants from ZIKV-infected cultures, whereas IFNα abundance was unchanged (Figures 3D and 3E). This analysis indicates differential activation of ISGs and IFN-I in ZIKV- and HSV-1-infected cultures.

To simultaneously measure IFN-I and ISG expression at single-cell level and with spatial resolution in infected brain organoids, we built a dual fluorescent reporter system. We engineered human embryonic stem cells (hESCs) to carry a GFP cassette driven by the *IFNB1* promoter (*IFN>GFP*) and a tdTomato cassette driven by the ISRE motif (*ISRE>tdT*) (Figure 3F). Immunostaining and flow cytometry analysis confirmed low basal expression of both reporters in control organoids and high *ISRE>tdT* expression in response to exogenous IFN-I (Figures S3C and S3D). To test the functionality of these reporters, we analyzed GFP and tdTomato expression by immunostaining in organoids stimulated with poly(I:C), a synthetic analog of double-stranded RNA (dsRNA) that acts as a potent IFN-I inducer in human NPCs (Lin et al., 2019). Consistent with induction, we detected high *IFN>GFP* and *ISRE>tdT* expression (Figures 3G–3J). However, this occurred only in 0.14% and 46% of the cells, respectively, fractions that were smaller than those measured in human lung epithelial A549 cells engineered with the same reporter system (3.6% and 91%, respectively; Figures S3E–S3G). These results validate the functionality of the dual reporter systems but reveal a high degree of stochasticity of *IFNB1* expression (Zhao et al., 2012) in brain organoids. We next analyzed reporter expression in response to viral infection by immunostaining. In tissues infected with ZIKV, we detected high *IFN>GFP* signals in very few cells (0.11%), indicating *IFNB1* expression in a rare population of cells, and high *ISRE>tdT* expression in 30% of cells (Figures 3K–3N), consistent with ISG induction. Spatial analysis of reporter expression in ZIKV-infected organoids revealed that *ISRE>tdT*-expressing cells, which co-expressed the neural progenitor marker Sox1 (Figures S3H and S3I), appeared in clusters (Figures 3K and S3H) and located in areas far from high *IFN>GFP*-expressing cells (Figure 3N). These observations point toward ISG expression in the absence of high IFN-I production, in line with an IFN-independent ISG induction model (Liu et al., 2019; Schneider et al., 2014). Furthermore, the fraction of *ISRE>tdT*-expressing cells located far from or close to high *IFN>GFP*-expressing cells in ZIKV-infected organoids was similar, in contrast to the distribution observed in organoids stimulated with poly(I:C) (Figures 3N and 3J), suggesting viral inhibition of paracrine IFN-I signaling. Consistent with this, expression of the IFN-I signaling transducer Stat2, which is targeted for degradation by ZIKV (Grant et al., 2016; Kumar et al., 2016), was reduced in ZIKV-infected regions compared with non-infected areas (Figure S3J). These observations suggest heterogenous and overall modest activation of the IFN-I response in ZIKV-infected organoids. In contrast to this, in HSV-1-infected organoids, we found high *IFN>GFP* and *ISRE>tdT* signals only in a very small fraction of cells (0.03% and 0.7%, respectively; Figures 3O–3R), indicating lack of IFN-I and ISG induction in most cells. These results reveal differential induction of the IFN-I system in organoids infected with ZIKV and HSV-1.

IFN-I response in brain organoids is more attenuated than in 2D cultures

Our finding that IFN-I induction is modest in infected brain organoids was surprising given the strong IFN-I production measured in 2D hNPC cultures (Ferraris et al., 2019; Lima et al., 2019; Simonin et al., 2016; Zhang et al., 2016) and non-neural cultures (Hamel et al., 2015; Li et al., 2017). To test whether the magnitude of the IFN-I response is influenced by the culture system or by the cell type composition, we compared the organoid response with the one of 2D cultures obtained from dissociation of brain organoids (disOrganoids; Figure S4A) and that of 2D cultures of non-neural cells such as A549. ZIKV and HSV-1 replicated efficiently in both 2D cultures, and these infections proceeded faster than in brain organoids (Figures S4B–S4E). qRT-PCR analysis at time points that showed similar ZIKV and HSV-1 infection levels across cultures revealed more prominent induction of *IFNA* and *IFNB1* in disOrganoids and A549 cells compared with the one measured in intact organoids (Figures 4A–4D). The only exception was induction of *IFNA* upon ZIKV infection, which was minimal in all tested culture systems (Figure 4A). Moreover, we analyzed the localization of Irf3, the major transcription factor that drives IFN-I transcription after nuclear translocation (Honda and Taniguchi, 2006), and found that the fraction of cells showing nuclear Irf3 accumulation was larger in disOrganoids and A549 cells compared with brain organoids (Figures 4E–4H and S4F). These results confirm a more attenuated activation of the IFN-I response in brain organoids compared with 2D cultures.

Efficient nuclear translocation of Irf3 relies on high expression of pattern recognition receptors (PRRs) mediating cytosolic virus sensing (Zhao et al., 2012). We found low expression of PRRs in early-stage organoids compared with later-stage organoids (Figure S4G), similar to the time-dependent expression timeline seen *in vivo* (Figure S4H). However, PRR expression in early-stage organoids was comparable with that measured in disOrganoids as well as in 2D cultures of NPCs, and the levels were lower than those measured in A549 cells (Figure 4I). All neural cultures (organoids, disOrganoids, and NPCs) also showed similar efficacy of Irf3 nuclear translocation upon poly(I:C) treatment, and this was lower than that of A549 cells (Figures 4I–4K and S4I). These

(G–R) Immunostaining (scale bars, 100 μm) of organoids generated from reporter cells and analyzed 1 day after stimulation with poly(I:C) (G) or after ZIKV or HSV-1 exposure (K and O). Dashed lines indicate organoid contour based on DAPI (data not shown). Insets (scale bars, 50 μm) represent a magnified view of the area close to one single *IFN>GFP*+ cell (arrows). Arrowheads indicate *ISRE>tdT*+ cells. Graphs are Tukey plots ($n \geq 3$; $p = 0.0211$ in H, $p = 0.0007$ in I, $p = 0.0068$ in J, $p = 0.0273$ in L, $p = 0.0091$ in M, $p = 0.3175$ in N, $p = 0.0857$ in P, $p = 0.6820$ in Q, $p = 0.5994$ in R; Mann-Whitney tests). Ctrl, control transfection.
See also Figure S3.

Please cite this article in press as: Krenn et al., Organoid modeling of Zika and herpes simplex virus 1 infections reveals virus-specific responses leading to microcephaly, Cell Stem Cell (2021), https://doi.org/10.1016/j.stem.2021.03.004

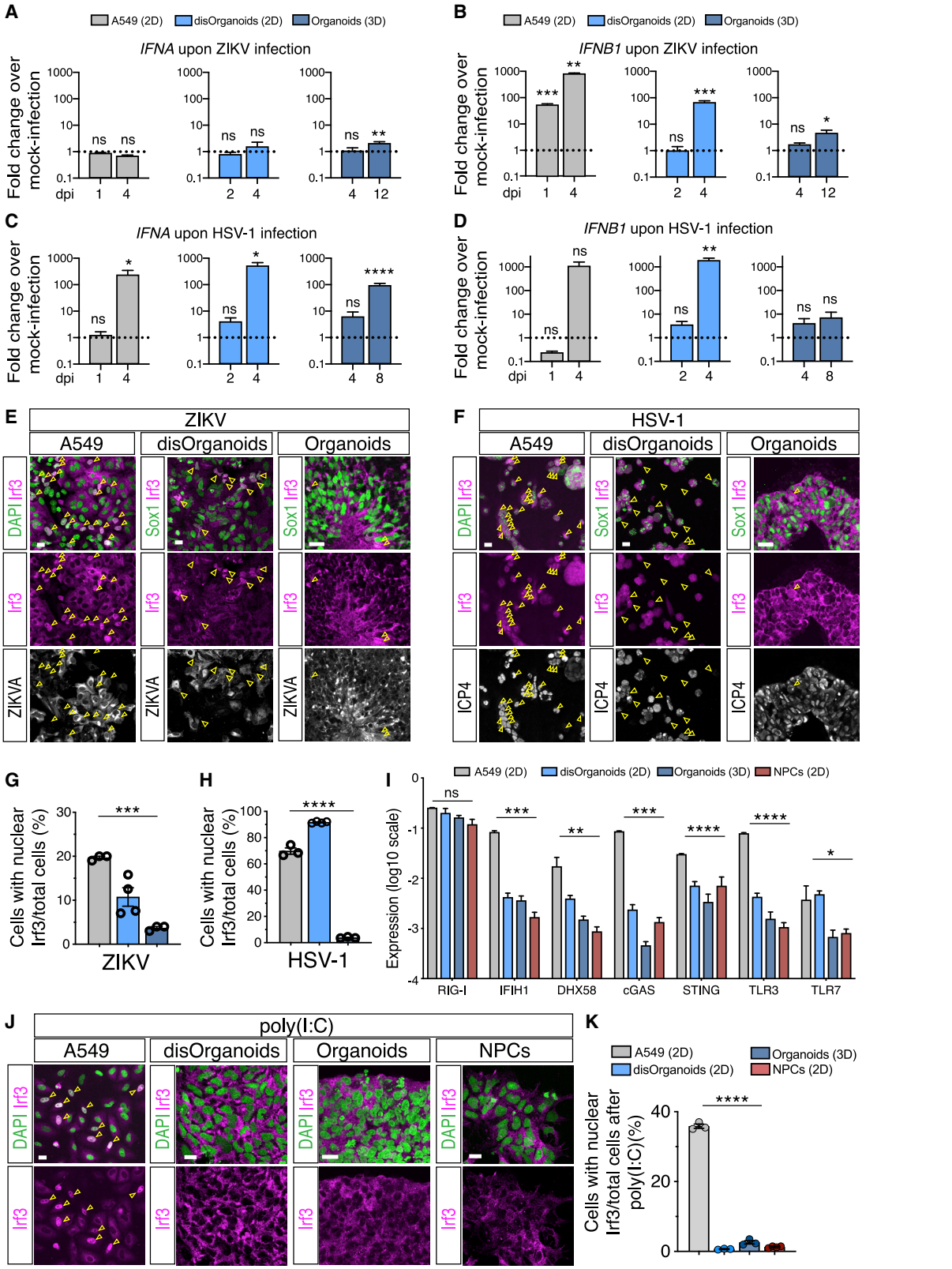

Figure 4. The IFN-I response in brain organoids is more attenuated than in 2D cultures

(A–D) Quantification of *IFNA* and *IFNB1* expression by qRT-PCR in cultures exposed to ZIKV (A and B) or HSV-1 (C and D). Dotted lines indicate a value of 1. Values are mean ± SEM (n = 3 for A549, n = 4 for disOrganoids, n = 7 for ZIKV Org, n = 3 for HSV-1 Org; ZIKV *IFNA*: p = 0.8985, A549, 1 dpi; p = 0.0823, A549, 4 dpi;

(legend continued on next page)

results suggest a cell type-specific modulation of virus sensing and argue against major changes in virus sensing between brain organoids and 2D neural cultures.

IFNβ treatment prevents ZIKV-induced organoid defects

The low levels of IFN-I measured in infected brain organoids could be responsible for their high susceptibility to ZIKV and HSV-1, despite some evidence suggesting that high IFN-I activity might exacerbate damage (Dang et al., 2016; Liu et al., 2019). Consistent with this, *ISRE>tdT* reporter expression correlated with lower levels of apoptosis in ZIKV-infected organoids (Figure S4J). To further demonstrate the neuroprotective effect of the IFN-I system in our infection models, we resorted to administration of exogenous IFN-I, which inhibits ZIKV and HSV-1 replication in monolayer cultures (Contreras and Arumugaswami, 2016; Härle et al., 2002; Lafaille et al., 2012; Hamel et al., 2015; Lin et al., 2019; Gobillot et al., 2020). We confirmed the ability of two IFN-I subtypes, IFNα2 and IFNβ, to restrict ZIKV and HSV-1 infections in 2D disOrganoid cultures (Figures S5A–S5D), in line with their similar signaling downstream of the IFN-I receptor (Ivashkiv and Donlin, 2014). Given the major differences in viral kinetics and in the strength of innate immune signaling observed in brain organoids and in 2D cultures, we investigated whether IFN-I treatment could also be efficacious in brain organoid models.

We first applied IFN-I treatments to organoids that had been exposed to ZIKV and found that they both significantly ameliorated ZIKV-induced growth defects (Figures 5A–C). IFN-I treatments were well tolerated because they did not compromise growth of mock-treated organoids or induce large-scale apoptosis (Figures S5E–S5I). Strikingly, immunohistochemistry analysis revealed that IFNβ treatment increased the area of VZ-like regions and reduced ZIKV infection, whereas IFNα2 showed much lower efficacy (Figures 5D and 5E). Poor efficacy of the IFNα2 treatment was unlikely to be due to lower biological activity because treatment with a higher dose of IFNα2 failed to further improve the rescue of ZIKV-infected cultures compared with the lower dose (Figure S5J). Also, neuroprotective activity was specific to IFN-I signaling because treatment with type III IFNs did not ameliorate the growth phenotype or induce ISG expression (Figures S5J and S5K). We then performed RNA sequencing on ZIKV-infected organoids treated with IFN-I. Principal-component analysis (PCA) and differential gene expression data revealed that IFNβ treatment completely reverted the transcriptional changes caused by ZIKV, whereas IFNα2 treatment only partially rescued gene expression (Figures 5F, 5G, and S5L), in line with our immunohistochemistry data. Moreover, IFNβ treatment reduced ZIKV vRNA expression levels already at 4 dpi and even more dramatically at 12 dpi, whereas IFNα2 treatment failed to do so (Figure 5H). These results reveal the neuroprotective function of the IFN-I system and the superiority of IFNβ over IFNα2 in ameliorating ZIKV-induced organoid defects.

IFNβ treatment fails to prevent HSV-1-induced organoid defects

We next tested the antiviral actions of IFNα2 and IFNβ against HSV-1 by comparing their ability to prevent growth and neuroepithelial defects in organoids that had been exposed previously to HSV-1 (Figure 6A). In contrast to the results obtained with ZIKV-infected organoids and HSV-1-infected 2D cultures, we found that only IFNα2 treatment ameliorated HSV-1-induced organoid growth defects (Figures 6B and 6C). Consistent with this, IFNα2 treatment improved organoid architecture, suppressed HSV-1 infection, and rescued Sox1 expression as well as N-cadherin localization, whereas IFNβ treatment failed to do so (Figures 6D–6G). Furthermore, transcriptional profiling of HSV-1-exposed cultures treated with IFN-I confirmed the inability of IFNβ treatment to rescue the transcriptional changes caused by HSV-1 (Figures 6H, 6I, and S6A). Moreover, analysis of HSV-1 transcript abundance measured by RNA sequencing confirmed that IFNα2 treatment efficiently suppressed HSV-1 transcription at 8 dpi and that IFNβ exerted a minor effect (Figure 6J). These results reveal the inability of IFNβ to perform its potent antiviral action against HSV-1, supporting differential functions of IFN-I subtypes in brain organoid models.

HSV-1 selectively inhibits IFNβ activity

The poor antiviral activity of IFNβ against HSV-1 could be due to its inability to induce a subset of ISGs counteracting HSV-1 compared with IFNα2. To identify such a subset of ISGs, we analyzed the differential expression signatures of (uninfected) organoids treated with IFNα2 or IFNβ compared with untreated samples. These were enriched in genes implicated in the defense response to viruses and in response to IFN-I (Figures S6B–S6D). In contrast with our hypothesis, we found that all DEGs induced by IFNα2 were also found in the IFNβ dataset and that the pattern of differential expression was remarkably similar, with the exception that IFNβ showed higher potency (Figures S6E and S6F). Even at later time points, the DEGs induced by IFNα2 largely overlapped with those upregulated in the IFNβ dataset. Noticeably though, differences in ISG levels and a time-dependent ISG downregulation specific to IFNα2-treated cultures and reminiscent of IFNα desensitization (Sandler et al.,

p = 0.6069, disOrganoids, 2 dpi; p = 0.9784, disOrganoids, 4 dpi; p = 0.7633, Org, 4 dpi; p = 0.0057, Org, 12 dpi; ZIKV *IFNB1*: p = 0.0005, A549, 1 dpi; p = 0.0015, A549, 4 dpi; p = 0.7036, disOrganoids, 2 dpi; p = 0.0008, disOrganoids, 4 dpi; p = 0.2135, Org, 4 dpi; p = 0.0333, Org, 12 dpi; HSV-1 *IFNA*: p = 0.5876, A549, 1 dpi; p = 0.0105, A549, 4 dpi; p = 0.1457, disOrganoids, 2 dpi; p = 0.0183, disOrganoids, 4 dpi; p = 0.2903, Org, 4 dpi; p < 0.0001, Org, 8 dpi; HSV-1 *IFNB1*: p = 0.0794, A549, 1 dpi; p = 0.1054, A549, 4 dpi; p = 0.3126, disOrganoids, 2 dpi; p = 0.0056, disOrganoids, 4 dpi; p = 0.4055, Org, 4 dpi; p = 0.2250, Org, 8 dpi; Mann-Whitney test comparisons of infected samples versus age-matched mock-treated samples). disOrganoids, dissociated Organoids; Org, organoids.

(E–H) Immunostaining (scale bars, 100 μm) and quantification of Irf3 nuclear localization. A549 and disOrganoids were analyzed at 4 dpi and organoids at 12 dpi (E) or 8 dpi (F). ICP4, infected cell polypeptide 4 protein of HSV-1. Color code as in (A). Values are mean ± SEM (p = 0.0007 in G; p < 0.0001 in H; one-way ANOVA).

(I) Expression of nucleic acid sensors measured by qRT-PCR. Values are mean ± SEM (n = 3, p = 0.3387, RIG-I; p = 0.0063, DHX58; p = 0.0432, TLR7; ****p < 0.0001; one-way ANOVA). RIG-I, retinoic acid inducible gene I.

(J and K) Immunostaining (scale bars, 20 μm) and quantification of Irf3 nuclear accumulation after poly(I:C) treatment. Values are mean ± SEM (n = 3, p < 0.0001, one-way ANOVA).

See also Figure S4.

Please cite this article in press as: Krenn et al., Organoid modeling of Zika and herpes simplex virus 1 infections reveals virus-specific responses leading to microcephaly, Cell Stem Cell (2021), https://doi.org/10.1016/j.stem.2021.03.004

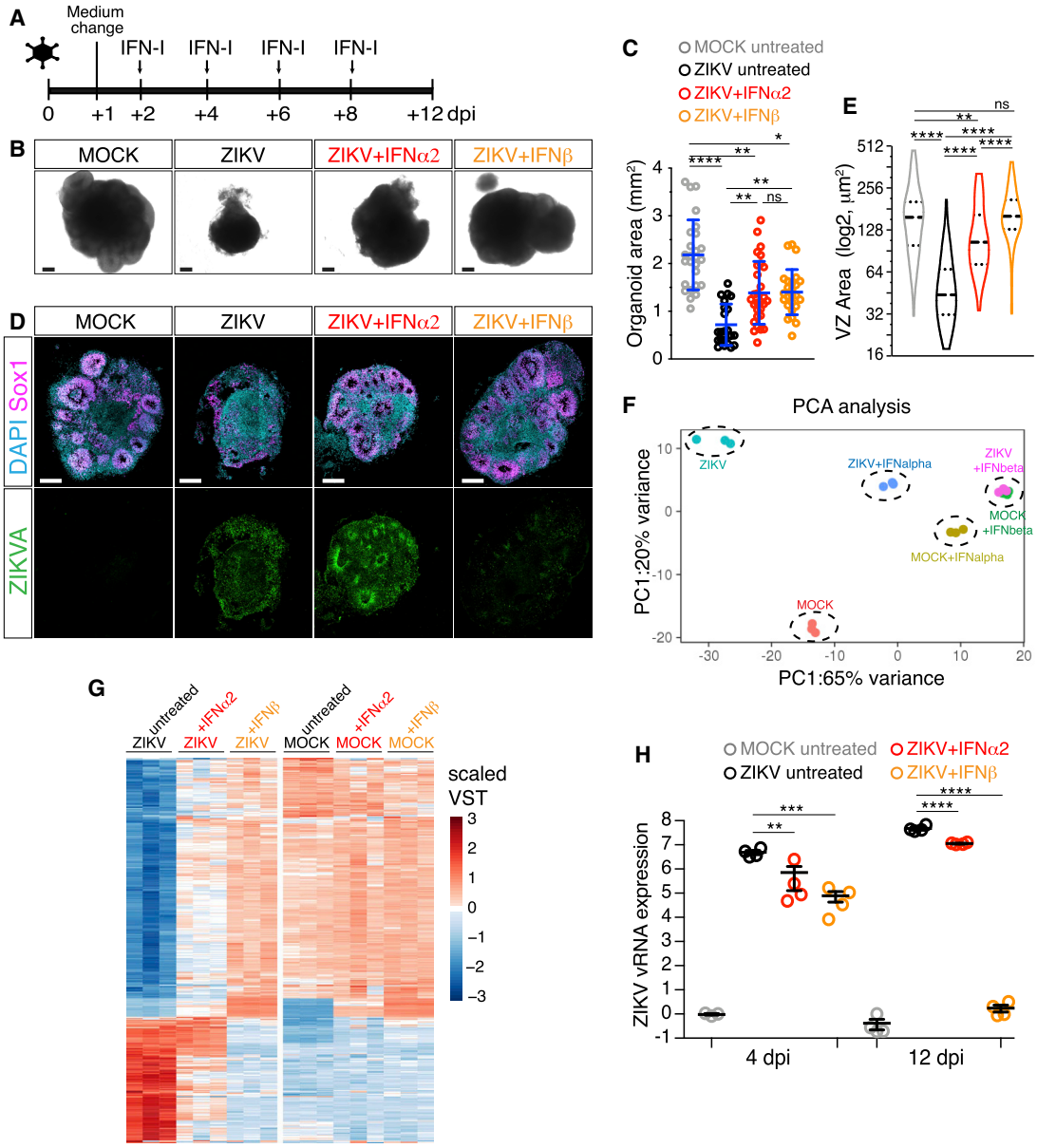

Figure 5. IFNβ treatment prevents ZIKV-induced organoid defects

(A) Timeline of interferon (IFN-I) treatment. Organoids were analyzed at 12 dpi.

(B and C) Images (scale bars, 200 µm) of organoids treated as in (A) and area quantification. Values are mean ± SD and represent individual organoids (****$p < 0.0001$; $p = 0.0063$, ZIKV+IFNα2 versus ZIKV; $p = 0.0021$, ZIKV+IFNβ versus ZIKV; $p > 0.9999$, ZIKV+IFNα2 versus ZIKV+IFNβ; $p = 0.0015$, ZIKV+IFNα2 versus mock treated; $p = 0.0117$, ZIKV+IFNβ versus mock-treated; Kruskal-Wallis test).

(D and E) Immunostaining (scale bars, 200 µm) of organoids and area quantification of VZ-like regions. Violin plots show median and quartiles (n = 114 regions from 6 mock-treated organoids, n = 55 from 7 ZIKV organoids, n = 73 from 7 ZIKV+IFNα2 organoids, n = 106 from 7 ZIKV+IFNβ organoids; $p = 0.0026$ ZIKV+IFNα2 versus mock treated; $p > 0.9999$ ZIKV+IFNβ versus mock treated; ****$p < 0.0001$; Kruskal-Wallis test).

(F and G) Principal-component analysis (PCA) and expression (in scaled variance stabilizing transformation [VST]) of DEGs.

(H) Quantification of ZIKV vRNA expression measured by qRT-PCR in organoids treated as in (A). Values are mean ± SEM (4 dpi: $p = 0.0017$ ZIKV+IFNα2 versus ZIKV, $p = 0.0005$ ZIKV+IFNβ versus ZIKV; ****$p < 0.0001$; one-way ANOVA, Tukey's multiple comparisons test).

See also Figure S5 and Table S2.

2014) became prominent (Figures S6G and S6H). These data argue against the existence of a set of ISGs uniquely induced by IFNα2, ruling out our hypothesis.

An alternative possibility is that HSV-1 might specifically block the activity of IFNβ through the action of one or multiple viral proteins (Danastas et al., 2020). Such an infection-dependent effect is supported by the observation that IFNβ showed potent antiviral activity against HSV-1 when administered to organoids before (but not after) viral exposure (Figures S7A and S7B), and by diminished IFNβ-dependent ISG expression in HSV-1-infected cultures

Please cite this article in press as: Krenn et al., Organoid modeling of Zika and herpes simplex virus 1 infections reveals virus-specific responses leading to microcephaly, Cell Stem Cell (2021), https://doi.org/10.1016/j.stem.2021.03.004

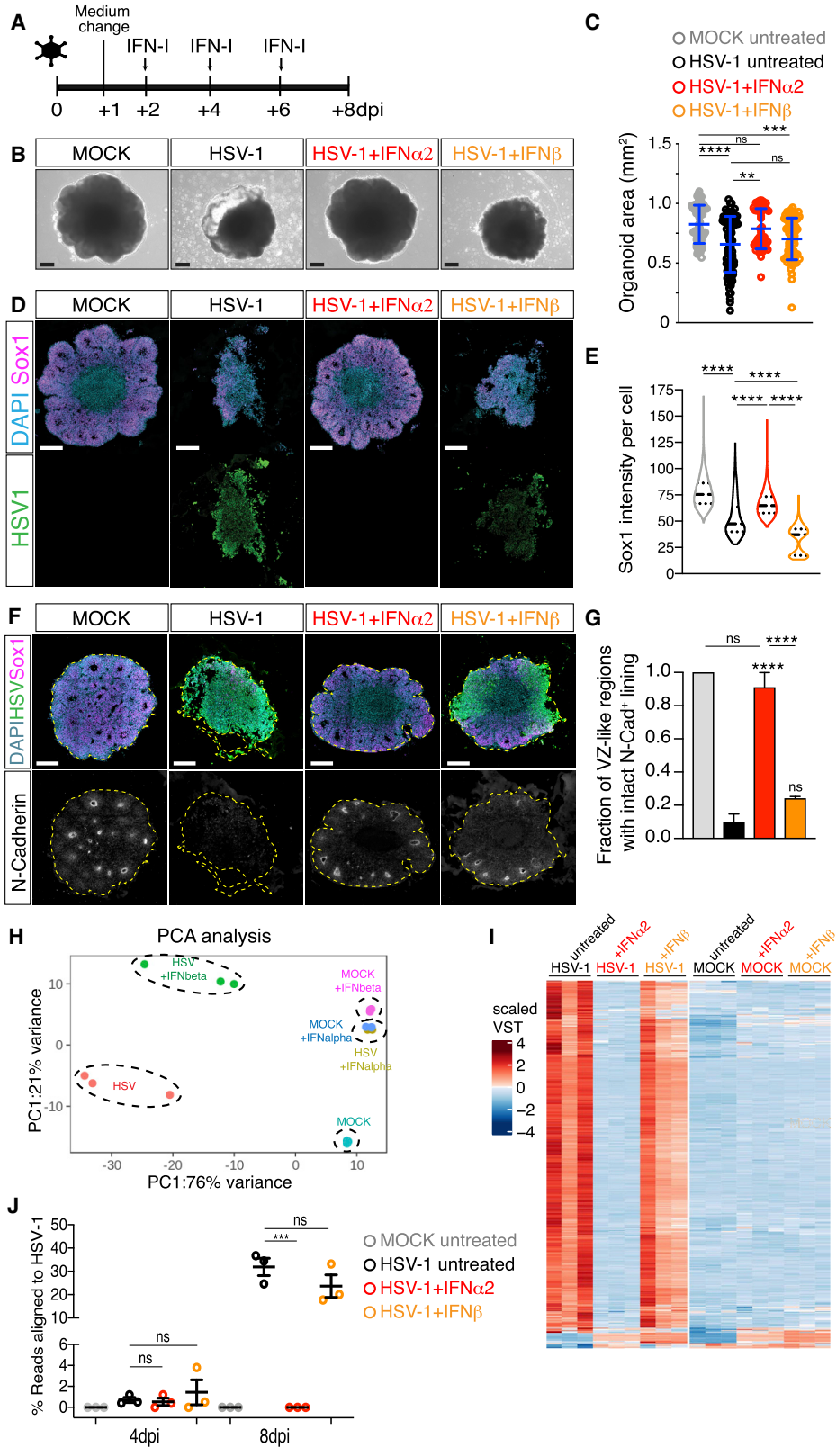

(legend on next page)

Please cite this article in press as: Krenn et al., Organoid modeling of Zika and herpes simplex virus 1 infections reveals virus-specific responses leading to microcephaly, Cell Stem Cell (2021), https://doi.org/10.1016/j.stem.2021.03.004

compared with mock-treated conditions (Figure S7C). We noticed that one of the affected ISGs was protein kinase R (PKR), an antiviral effector that inhibits translation of viral mRNAs by phosphorylating eIF2a (Schneider et al., 2014) and whose activity is counteracted by the HSV-1 protein ICP34.5 (Chou et al., 1995). This observation led us to hypothesize that the HSV-1 protein ICP34.5 may counteract IFNβ activity by targeting the PKR pathway. This model predicts that loss of ICP34.5 would render HSV-1 sensitive to IFNβ. We thus performed infections with an HSV-1 mutant strain that carries deletion of both copies of the ICP34.5 genes and is referred to as R3616 (Figure S7D; Chou et al., 1990). ICP34.5-null mutants replicate well in cell culture but they are attenuated in the brains of mice and humans (Bolovan et al., 1994; Chou et al., 1990; Kaur et al., 2012; Leib et al., 1999). Consistent with *in vivo* neuroattenuation, the ICP34.5-null strain R3616 reduced organoid growth less efficiently than wild-type (WT) HSV-1, especially at the low inoculum dose, and exhibited limited viral spreading and viral particle release compared with WT HSV-1 (Figures 7A–7I). Importantly, when R3616 showed prominent infection, its replication was blocked efficiently by IFNβ (Figure 7J-M), consistent with our prediction. R3616 infection did not change the expression levels of ISGs similar to WT HSV-1, ruling out a direct role of ICP34.5 in ISG induction (Figure S7E). These results indicate that HSV-1 selectively inhibits IFNβ action in part via ICP34.5.

DISCUSSION

Here we establish human brain organoid models for two distinct TORCH viruses, ZIKV and HSV-1. We show that these two models share features of microcephaly but exhibit major differences in the underlying structural defects and transcriptional profiles as well as in engagement of the antiviral system and sensitivity to IFN-I. These results argue for the existence of unique pathogenic mechanisms underlying virus-induced microcephaly and for the use of tailored antiviral strategies against TORCH pathogens.

ZIKV and HSV-1 infect hNPCs, leading to productive infection and causing reduced organoid size and cell depletion. These data implicate hNPC infection in TORCH neuropathogenesis and are consistent with other organoid models of ZIKV and HSV-1 infection (Cugola et al., 2016; Gabriel et al., 2017; Garcez et al., 2016; Qian et al., 2016; Qiao et al., 2020; Watanabe et al., 2017) as well as with clinical findings associated with virus exposure in the first and second trimesters of pregnancy (Honein et al., 2017; Marquez et al., 2011). HSV-1 infection in organoids appears to be more destructive than that caused by ZIKV, in line with the high severity of *in utero* HSV infections (Marquez et al., 2011). In contrast to this, HCMV shows limited tropism for primitive hNPCs and poor replication in early-stage organoids. This phenotype is likely due to the lack of intermediate progenitors (Kanton et al., 2019), a population of hNPCs identified recently as the major cellular target of HCMV in a 45-day-old organoid model of microcephaly (Sun et al., 2020). These data suggest a different neurotropism of TORCH viruses in the human fetal brain.

Mechanistically, we show that ZIKV and HSV-1 infections trigger apoptosis, as reported previously (Cairns et al., 2020; Cugola et al., 2016; Hanners et al., 2016; Qian et al., 2016; Souza et al., 2016; Watanabe et al., 2017; Chucair-Elliott et al., 2014). Apoptosis likely represents a general cellular defense against viral spreading that could explain the neurotoxicity of congenital TORCH infections. However, our analysis of apoptosis and lumen size suggests that different mechanisms of tissue damage may be involved. Although ZIKV infection reduces lumen size likely by basal delamination of apoptotic cells from the neuroepithelium, HSV-1 infection results in enlarged lumens, possibly through apical extrusion of apoptotic cells. Furthermore, our data suggest that HSV-1 is unique in its ability to cause neuropathology by impairing neuroepithelial integrity, in line with the key roles of cell adhesion in controlling NPC proliferation and maintenance during brain development (Chenn and Walsh, 2002; Hatakeyama et al., 2014; Kadowaki et al., 2007; Rousso et al., 2012). HSV-1 may perturb neuroepithelial polarity by promoting N-cadherin cleavage (Reiss et al., 2005) or by disrupting adherens junctions by binding to the cell adhesion molecule Nectin1 (Krummenacher et al., 2003; Richart et al., 2003; Simpson et al., 2005). Remarkably, these cytoarchitectural changes seen in organoids are distinct from the large multicellular structures observed in 2D neural cultures (this study and Cairns et al., 2020). These discrepancies are likely due to major changes in cell adhesion and polarity of NPCs grown in monolayer and 3D organoid cultures (Scuderi et al., 2021), confirming the superiority of brain organoids in mimicking the neuropathological features associated with HSV-1 infection.

The structural and cellular differences of ZIKV and HSV-1 organoid models are also reflected in their transcriptional profiles. Although cell death is concomitant with activation of cellular stress- and virus defense-related pathways in ZIKV-infected

Figure 6. IFNβ treatment fails to prevent HSV-1-induced organoid defects

(A) Timeline of IFN-I administration. Organoids were analyzed at 8 dpi.

(B and C) Images (scale bars, 200 μm) and area quantification of organoids treated as in (A). Values are mean ± SD (****$p < 0.0001$; $p = 0.0043$, HSV+IFNα2 versus HSV; $p > 0.9999$, HSV+IFNβ versus HSV; $p = 0.0587$, HSV+IFNα2 versus HSV+IFNβ; $p > 0.9999$, HSV+IFNα2 versus mock treated; $p = 0.0007$, HSV+IFNβ versus mock treated; Kruskal-Wallis test).

(D and F) Immunostaining (scale bars, 200 μm) of organoids. Dashed lines indicate organoid contour.

(E) Quantification of Sox1 mean intensity per cell. Violin plots show medians and quartiles ($n > 3,000$ cells from at least 3 organoids per condition, ****$p < 0.0001$, Kruskal-Wallis test).

(G) Quantification of the VZ-like regions marked by N-Cadherin (N-Cad) apical accumulation. Data are mean ± SEM ($n = 3$ experiments; ****$p < 0.0001$; ns, $p > 0.9999$; Kruskal-Wallis test).

(H and I) PCA and expression (in scaled VST) of genes differentially expressed in HSV-1-infected organoids.

(J) Percentage of RNA sequencing reads aligned to the HSV-1 genomic sequence. Values are mean ± SEM (for 4 dpi: $p = 0.8613$, mock treated versus HSV; $p = 0.9975$, HSV+IFNα2 versus HSV; $p = 0.8447$, HSV+IFNβ versus HSV; for 8 dpi: $p = 0.003$, mock treated versus HSV; $p = 0.0003$, HSV+IFNα2 versus HSV; $p = 0.2943$, HSV+IFNβ versus HSV; one-way ANOVA, Tukey's multiple comparisons test).

See also Figure S6 and Table S2.

Please cite this article in press as: Krenn et al., Organoid modeling of Zika and herpes simplex virus 1 infections reveals virus-specific responses leading to microcephaly, Cell Stem Cell (2021), https://doi.org/10.1016/j.stem.2021.03.004

CellPress

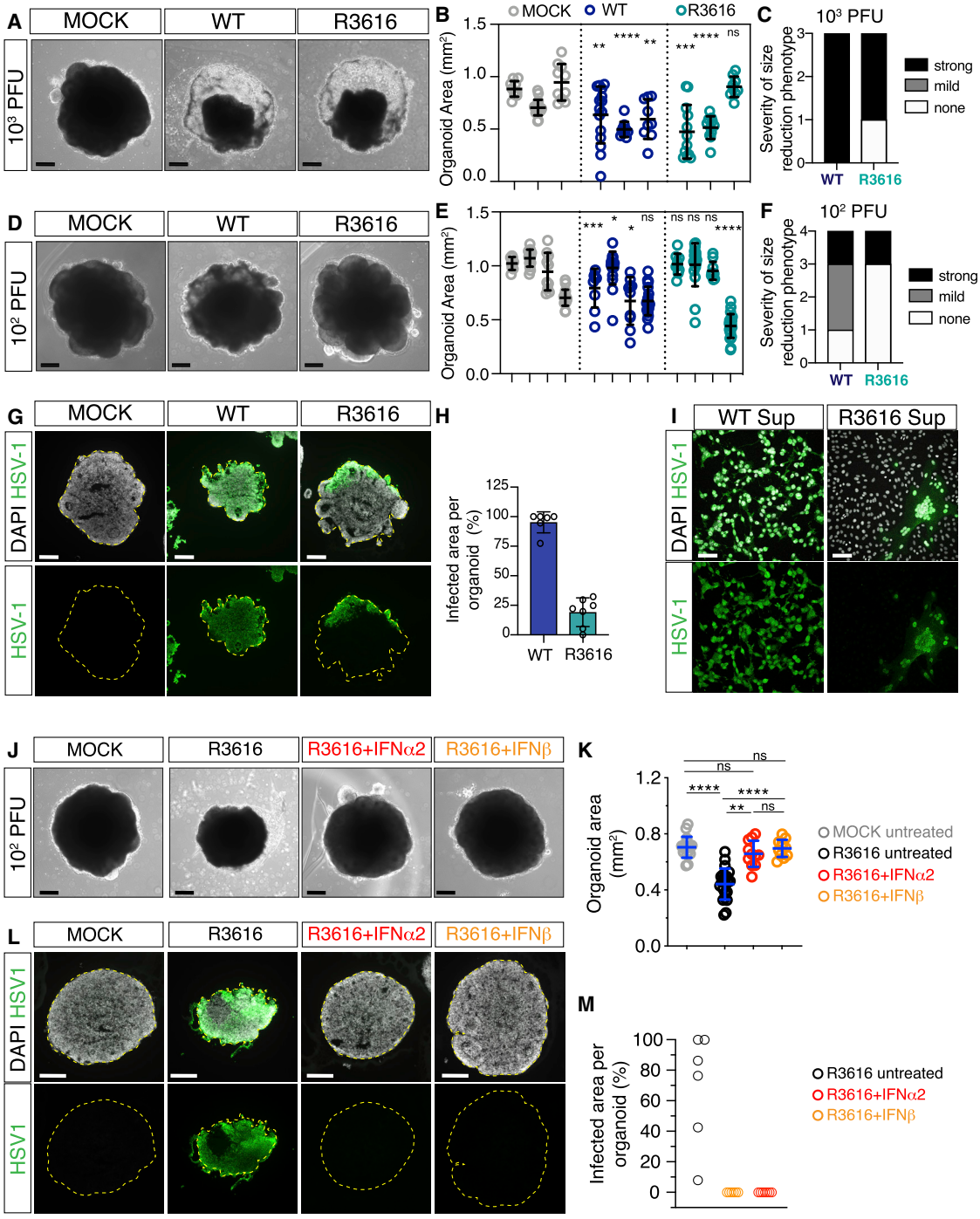

Figure 7. HSV-1 selectively counteracts IFNβ activity

(A–F) Images (scale bars, 200 μm) and area quantifications of organoids exposed to HSV-1 wild-type (WT), R3616 mutant, or mock treated and analyzed at 8 dpi. Values are mean ± SD and represent individual organoids (in B: for WT, p = 0.0066 and p = 0.0021; for R3616, p = 0.0008 and p = 0.7802; in E: for WT, p = 0.0002, p = 0.02, p = 0.0232, and p = 0.1606; for R3616, p = 0.8148, p = 0.5701, and p = 0.7394; ****p < 0.0001; Mann-Whitney test comparisons with mock-treated counterparts). The outcomes of the infection experiments in (C) and (F) are based on statistical significance (strong when $p < 0.005$, mild when $0.005 < p < 0.05$, or none when $p > 0.05$).

(G–H) Immunostaining (scale bars, 200 μm) and quantification of infected organoid area at 8 dpi. Dashed lines indicate organoid contour. Data are mean ± SD (n = 6 organoids for WT, n = 7 for R3616).

(I) Immunostaining (scale bars, 100 μm) of Vero cells incubated with sups from HSV-1 WT- or R3616-infected organoids at 8 dpi.

(legend continued on next page)

Please cite this article in press as: Krenn et al., Organoid modeling of Zika and herpes simplex virus 1 infections reveals virus-specific responses leading to microcephaly, Cell Stem Cell (2021), https://doi.org/10.1016/j.stem.2021.03.004

cultures, in agreement with previous studies (Gladwyn-Ng et al., 2018; Liu et al., 2019; Watanabe et al., 2017), apoptosis is linked to upregulation of the ATF and Jun/Fos families of transcription factors and activation of non-neural developmental pathways in HSV-1-infected cultures. In the case of HSV-1, it is possible that this transcriptional activation is required to ensure efficient replication because HSV-1 induces similar profiles in other cells (Drayman et al., 2019; Hensel et al., 2019; Hu et al., 2016). Another option is that deregulation of non-neural genes caused by HSV-1 could contribute to loss of neuroepithelial identity. Indeed, the altered hNPC morphology, reduced apical N-cadherin localization, and disintegration of infected organoids are reminiscent of the morphological changes, lowered cadherin levels, and weakened adhesion of mesenchymal cells (Thiery et al., 2009).

Our work highlights major differences in the cellular innate response against ZIKV and HSV-1 and their sensitivity to IFN-I. Although these disparities are perhaps not surprising, given the great diversity of the two viruses, these phenotypes are unique to brain organoids. We show that ZIKV and HSV-1 infections of organoids attenuate IFN-I responses much more strongly compared with 2D cultures, helping resolve a discrepancy in the field regarding the magnitude of the antiviral response between 2D and 3D culture systems (Li et al., 2017; Lima et al., 2019; Liu et al., 2019; Simonin et al., 2016; Zhang et al., 2016). The attenuated IFN-I response of organoids is consistent with the low immune reactions described in the microcephalic brains of ZIKV-infected patients (Lima et al., 2019) and with the generally low IFN-I activity of the brain (Sorgeloos et al., 2013). Changes in the modulation of innate immune reactions between 3D and 2D culture systems may result from differences in infectivity levels and/or viral spreading because we observed lower initial infection levels and much slower kinetics of viral replication in 3D compared with 2D culture. Slow kinetics often reflect a small fraction of infected cells and could thus explain the rare activation of IFNβ transcription measured by our reporter assay. These discrepancies could result from inefficient cell targeting because of limited cell surface accessibility and/or from reduced local spreading because of stronger cell-to-cell contacts in 3D compared with 2D culture.

Moreover, our work reveals that ZIKV and HSV-1 replication in organoid cultures is differentially sensitive to the action of distinct IFN-I subtypes. These results lend support to the neuroprotective function of the IFN-I system against viral infections (Gorman et al., 2018; Leib et al., 1999; Li et al., 2017; Lin et al., 2019; Sorgeloos et al., 2013; Wang et al., 2012) and to the view that distinct IFN subtypes can mediate different biological outcomes (Ng et al., 2016). Nevertheless, it is surprising that distinct IFN-dependent viral phenotypes are detectable in 3D while remaining indistinguishable in 2D cultures (this study and Contreras and Arumugaswami, 2016; Härle et al., 2002; Lafaille et al., 2012). A contributing factor could be the duration of the IFN-I treatment because the pattern of ISG expression induced by IFNα/β starts to differ after repeated administrations. Viral phenotypes in 3D culture might also be strongly influenced by viral immune evasion mechanisms (Chou et al., 1990; Danastas et al., 2020; Gorman et al., 2018; Grant et al., 2016; Kumar et al., 2016). The reduced efficacy of IFN-I against ZIKV in 3D versus 2D culture, the neuroattenuation of the ICP34.5-null HSV-1 mutant, and the poor IFNβ activity against HSV-1 in brain organoids are compatible with this possibility.

Finally, our work uncovers the existence of previously unappreciated differences in IFN-I activities. The superior antiviral activity of IFNβ over IFNα2 against ZIKV infection likely reflects the longer-lasting and more potent ISG induction by IFNβ over IFNα2, in line with the higher potency of IFNβ (Bolen et al., 2014; Gobillot et al., 2020). More intriguing is the poor antiviral activity of IFNβ against HSV-1 because this effect could be specific to the brain. In fact, IFNβ potently inhibits HSV-1 replication in other cells and in mice (Arao et al., 1997; Carr et al., 2003; Giraldo et al., 2020; Härle et al., 2001). Our pre- and post-treatment IFNβ experiments with WT and ICP34.5-null HSV-1 viruses indicate that HSV-1 selectively neutralizes IFNβ action, in line with the well-described ability of HSV-1 to evade IFN-I signaling (Danastas et al., 2020). This mechanism may be an efficient strategy to target the most potent IFN type in the brain when IFNα species and IFNβ are produced (Sorgeloos et al., 2013). Our results suggest that such an evasion mechanism is mediated in part by the viral protein ICP34.5, which possibly counteracts ISG induction and PKR activity downstream of IFN-I signaling (Chou et al., 1995; He et al., 1997). However, because PKR is induced and likely also activated in IFNα2-treated organoids, future work is needed to characterize the mechanisms determining the selectivity against IFNβ.

In conclusion, the organoid infection models described in this work have a great utility for evaluating therapeutic agents against ZIKV and HSV-1 and can serve as experimental platforms for better characterizing the activity of human IFNs. Although our results support a therapeutic use of specific IFN-I against ZIKV and HSV-1 infection, our understanding of IFN activities in humans is limited, as reflected in the toxicity and efficacy issues of IFN-based therapies (Fritz-French and Tyor, 2012; Li et al., 2018). Mechanistic studies of ISG function in these organoid infection systems will help guide the design of more efficacious IFN-I modulatory compounds. Our infection models for HSV-1 could serve as platforms for further characterization of HSV-1 evasion mechanisms and for testing of HSV-1 mutants. This work will help improve the design of oncolytic HSV-1 vectors for glioblastoma therapy that could overcome the limited efficacy of current HSV-1 viruses (Kaur et al., 2012). More broadly, our work calls for a paradigm shift to human 3D systems for study of viral mechanisms that will be instrumental for development of more effective antiviral compounds for treatment of neurological complications.

Limitations of study

Our analysis of antiviral signaling is limited by the small number of antiviral genes analyzed and by the lack of time-resolved

(J–M) Images, immunostaining (scale bars, 200 μm), and quantification of organoid infected area at 8 dpi. Refer to Figure 6 for comparison with WT HSV-1. Values in (K) are mean ± SD (n = 6 untreated organoids, n = 7 organoids for IFNα2 and IFNβ; ****$p < 0.0001$; ns, $p > 0.9999$; $p = 0.0020$ R3616+IFNα2 versus R3616; Kruskal-Wallis test). ns, non-significant.
See also Figure S7 and Tables S1 and S2.

tissue dynamics of viral and host protein expression. Such analyses in large 3D tissue-like brain organoids are technically challenging, and application of emerging techniques, such as spatial transcriptomics (Burgess, 2019) and live 3D tissue fluorescence imaging (Rios and Clevers, 2018) in an appropriate biosafety setting, will allow greater insights into the tissue dynamics of viral spreading and antiviral signaling. Another limitation of the organoid models used in this study is their low cellular complexity, which does not recapitulate the full repertoire of neural cells seen in late-stage organoid cultures (Kanton et al., 2019), and their lack of microglia, a limitation of current organoid models (Amin and Paşca, 2018). The development of co-culture systems of late-stage organoid cultures and microglia will be instrumental to better recapitulate fetal neuroimmune interactions that could be relevant for viral pathogenesis.

STAR★METHODS

Detailed methods are provided in the online version of this paper and include the following:

- KEY RESOURCES TABLE
- RESOURCE AVAILABILITY
  - Lead contact
  - Materials availability
  - Data and code availability
- EXPERIMENTAL MODEL AND SUBJECT DETAILS
  - Human embryonic stem cells and cell lines
  - Viruses
- METHOD DETAILS
  - Maintenance of hESCs
  - Generation of interferon reporter lines
  - Generation of cerebral organoids
  - Generation of 2D neural cultures
  - Infection of cerebral organoids
  - Infection of 2D cultures
  - Interferon and poly(I:C) treatments
  - Cryo-sectioning, immunostaining and imaging
  - Quantification of cytokine levels by ELISA
  - RNA extraction and RT-qPCR analysis
  - RNA-sequencing and analysis
  - Quantification of apoptosis
  - Quantification of Sox1 levels
  - Quantification of IFN > GFP and ISRE > tdTomato positive cells
  - PCR on viral nucleic acids
- QUANTIFICATION AND STATISTICAL ANALYSIS

SUPPLEMENTAL INFORMATION

Supplemental information can be found online at https://doi.org/10.1016/j.stem.2021.03.004.

ACKNOWLEDGMENTS

We thank all members of the Knoblich laboratory for technical expertise and feedback. We thank the Organoid research unit, Lena Schwarz, and Paul Möseneder for technical support; the IMBA/IMP BioOptics facility for flow cytometry and microscopy services; IMP/IMBA Bioinformatics for sequencing analysis; A. Kavirayani and the VBCF HistoPathology facility (http://www.viennabiocenter.org/facilities) for histological support and consultation; and A. Sommer and the VBCF Sequencing unit (http://www.viennabiocenter.org/facilities) for sequencing. We also thank the EVAg project, Anna Obenauf (IMP, Austria), and Luka Cicin-Sain (Helmholtz Centre for Infection Research, Germany) for providing reagents. V.K. received funding from an EMBO fellowship (ALTF 1312-2015) and from the European Union Horizon 2020 Research and Innovation Program under Marie Skłodowska-Curie grant agreement 703112. C.B. is a member of the VBC doctoral program. Work in U.K.'s laboratory is supported by Helmholtz Zukunftthema "Immunology & Inflammation" (ZT-0027). Work in A.M.'s laboratory is supported by the Swedish Research Council (2018-05766). Work in J.A.K.'s laboratory is supported by the Austrian Federal Ministry of Education, Science and Research; the Austrian Academy of Sciences; the City of Vienna; the Austrian Science Fund (special research programs F78 Stem Cell, F 7803-B, and SFB-F78 P04); and a European Research Council advanced grant under the European Union Horizon 2020 Program (695642).

AUTHOR CONTRIBUTIONS

V.K. and J.A.K. conceived the project and wrote the manuscript with input from all authors. V.K. performed experiments and collected and analyzed the data with help from C.B. T.R.B. performed bioinformatic analysis. J.S. and U.K. contributed to conceptualization of the project and provided reagents and technical expertise. A.C., C.S., and A.M. contributed reagents and technical expertise. R.R.C. and P.P.G. helped with experimental design and data interpretation. J.A.K. acquired funding.

DECLARATION OF INTERESTS

J.A.K. is inventor on a patent describing cerebral organoid technology and co-founder and scientific advisory board member of a:head bio AG.

Received: May 14, 2020
Revised: December 7, 2020
Accepted: March 4, 2021
Published: April 9, 2021

SUPPORTING CITATIONS

The following references appear in the Supplemental information: Ferenczy and DeLuca (2009); Lanciotti et al. (2008); Miller et al. (2014); Paijo et al. (2016).

REFERENCES

Aho, V., Myllys, M., Ruokolainen, V., Hakanen, S., Mäntylä, E., Virtanen, J., Hukkanen, V., Kühn, T., Timonen, J., Mattila, K., et al. (2017). Chromatin organization regulates viral egress dynamics. Sci. Rep. *7*, 3692.

Amin, N.D., and Paşca, S.P. (2018). Building Models of Brain Disorders with Three-Dimensional Organoids. Neuron *100*, 389–405.

Anders, S., Pyl, P.T., and Huber, W. (2015). HTSeq–a Python framework to work with high-throughput sequencing data. Bioinformatics *31*, 166–169.

Anderson, T., and Humphreys, G. (2019). Zika: The Continuing Threat. Bull. World Health Organ. *97*, 6–7.

Arao, Y., Ando, Y., Narita, M., and Kurata, T. (1997). Unexpected correlation in the sensitivity of 19 herpes simplex virus strains to types I and II interferons. J. Interferon Cytokine Res. *17*, 537–541.

Bagley, J.A., Reumann, D., Bian, S., Lévi-Strauss, J., and Knoblich, J.A. (2017). Fused cerebral organoids model interactions between brain regions. Nat. Methods *14*, 743–751.

Baker, B.M., and Chen, C.S. (2012). Deconstructing the third dimension: how 3D culture microenvironments alter cellular cues. J. Cell Sci. *125*, 3015–3024.

Bale, J.F., Jr., and Murph, J.R. (1992). Congenital infections and the nervous system. Pediatr. Clin. North Am. *39*, 669–690.

Bolen, C.R., Ding, S., Robek, M.D., and Kleinstein, S.H. (2014). Dynamic expression profiling of type I and type III interferon-stimulated hepatocytes reveals a stable hierarchy of gene expression. Hepatology *59*, 1262–1272.

Bolovan, C.A., Sawtell, N.M., and Thompson, R.L. (1994). ICP34.5 mutants of herpes simplex virus type 1 strain 17syn+ are attenuated for neurovirulence in

mice and for replication in confluent primary mouse embryo cell cultures. J. Virol. *68*, 48–55.

Bower, J.R., Mao, H., Durishin, C., Rozenbom, E., Detwiler, M., Rempinski, D., Karban, T.L., and Rosenthal, K.S. (1999). Intrastrain variants of herpes simplex virus type 1 isolated from a neonate with fatal disseminated infection differ in the ICP34.5 gene, glycoprotein processing, and neuroinvasiveness. J. Virol. *73*, 3843–3853.

Brasil, P., Pereira, J.P., Raja Gabaglia, C., Damasceno, L., Wakimoto, M., Ribeiro Nogueira, R.M., Carvalho de Sequeira, P., Machado Siqueira, A., Abreu de Carvalho, L.M., Cotrim da Cunha, D., et al. (2016). Zika Virus Infection in Pregnant Women in Rio de Janeiro - Preliminary Report. N. Engl. J. Med. *375*, 2321–2334.

Bray, N.L., Pimentel, H., Melsted, P., and Pachter, L. (2016). Near-optimal probabilistic RNA-seq quantification. Nat. Biotechnol. *34*, 525–527.

Brown, R.M., Rana, P.S.J.B., Jaeger, H.K., O'Dowd, J.M., Balemba, O.B., and Fortunato, E.A. (2019). Human Cytomegalovirus Compromises Development of Cerebral Organoids. J. Virol. *93*, e00957-19.

Burgess, D.J. (2019). Spatial transcriptomics coming of age. Nat. Rev. Genet. *20*, 317.

Cairns, D.M., Rouleau, N., Parker, R.N., Walsh, K.G., Gehrke, L., and Kaplan, D.L. (2020). A 3D human brain-like tissue model of herpes-induced Alzheimer's disease. Sci. Adv. *6*, eaay8828.

Calistri, A., Parolin, C., and Palù, G. (2003). Herpes simplex virus type 1 can either suppress or enhance human immunodeficiency virus type 1 replication in CD4-positive T lymphocytes. J. Med. Virol. *70*, 163–170.

Carr, D.J.J., Al-khatib, K., James, C.M., and Silverman, R. (2003). Interferon-beta suppresses herpes simplex virus type 1 replication in trigeminal ganglion cells through an RNase L-dependent pathway. J. Neuroimmunol. *141*, 40–46.

Carver, E.A., Jiang, R., Lan, Y., Oram, K.F., and Gridley, T. (2001). The mouse snail gene encodes a key regulator of the epithelial-mesenchymal transition. Mol. Cell. Biol. *21*, 8184–8188.

Cheeran, M.C.-J., Lokensgard, J.R., and Schleiss, M.R. (2009). Neuropathogenesis of congenital cytomegalovirus infection: disease mechanisms and prospects for intervention. Clin. Microbiol. Rev. *22*, 99–126.

Chenn, A., and Walsh, C.A. (2002). Regulation of cerebral cortical size by control of cell cycle exit in neural precursors. Science *297*, 365–369.

Chou, J., Kern, E.R., Whitley, R.J., and Roizman, B. (1990). Mapping of herpes simplex virus-1 neurovirulence to gamma 134.5, a gene nonessential for growth in culture. Science *250*, 1262–1266.

Chou, J., Chen, J.J., Gross, M., and Roizman, B. (1995). Association of a M(r) 90,000 phosphoprotein with protein kinase PKR in cells exhibiting enhanced phosphorylation of translation initiation factor eIF-2 alpha and premature shutoff of protein synthesis after infection with gamma 134.5- mutants of herpes simplex virus 1. Proc. Natl. Acad. Sci. USA *92*, 10516–10520.

Chucair-Elliott, A.J., Conrady, C., Zheng, M., Kroll, C.M., Lane, T.E., and Carr, D.J.J. (2014). Microglia-induced IL-6 protects against neuronal loss following HSV-1 infection of neural progenitor cells. Glia *62*, 1418–1434.

Contreras, D., and Arumugaswami, V. (2016). Zika Virus Infectious Cell Culture System and the In Vitro Prophylactic Effect of Interferons. J. Vis. Exp. (114), 54767.

Coyne, C.B., and Lazear, H.M. (2016). Zika virus - reigniting the TORCH. Nat. Rev. Microbiol. *14*, 707–715.

Cugola, F.R., Fernandes, I.R., Russo, F.B., Freitas, B.C., Dias, J.L.M., Guimarães, K.P., Benazzato, C., Almeida, N., Pignatari, G.C., Romero, S., et al. (2016). The Brazilian Zika virus strain causes birth defects in experimental models. Nature *534*, 267–271.

Danastas, K., Miranda-Saksena, M., and Cunningham, A.L. (2020). Herpes Simplex Virus Type 1 Interactions with the Interferon System. Int. J. Mol. Sci. *21*, 5150.

Dang, J., Tiwari, S.K., Lichinchi, G., Qin, Y., Patil, V.S., Eroshkin, A.M., and Rana, T.M. (2016). Zika Virus Depletes Neural Progenitors in Human Cerebral Organoids through Activation of the Innate Immune Receptor TLR3. Cell Stem Cell *19*, 258–265.

Di Lullo, E., and Kriegstein, A.R. (2017). The use of brain organoids to investigate neural development and disease. Nat. Rev. Neurosci. *18*, 573–584.

Drayman, N., Patel, P., Vistain, L., and Tay, S. (2019). HSV-1 single-cell analysis reveals the activation of anti-viral and developmental programs in distinct sub-populations. eLife *8*, 2503.

Duval, K., Grover, H., Han, L.-H., Mou, Y., Pegoraro, A.F., Fredberg, J., and Chen, Z. (2017). Modeling Physiological Events in 2D vs. 3D Cell Culture. Physiology (Bethesda) *32*, 266–277.

Ferenczy, M.W., and DeLuca, N.A. (2009). Epigenetic modulation of gene expression from quiescent herpes simplex virus genomes. J. Virol. *83*, 8514–8524.

Ferraris, P., Cochet, M., Hamel, R., Gladwyn-Ng, I., Alfano, C., Diop, F., Garcia, D., Talignani, L., Montero-Menei, C.N., Nougairède, A., et al. (2019). Zika virus differentially infects human neural progenitor cells according to their state of differentiation and dysregulates neurogenesis through the Notch pathway. Emerg. Microbes Infect. *8*, 1003–1016.

Francis, K., and Palsson, B.O. (1997). Effective intercellular communication distances are determined by the relative time constants for cyto/chemokine secretion and diffusion. Proc. Natl. Acad. Sci. USA *94*, 12258–12262.

Fritz-French, C., and Tyor, W. (2012). Interferon-α (IFNα) neurotoxicity. Cytokine Growth Factor Rev. *23*, 7–14.

Gabriel, E., Ramani, A., Karow, U., Gottardo, M., Natarajan, K., Gooi, L.M., Goranci-Buzhala, G., Krut, O., Peters, F., Nikolic, M., et al. (2017). Recent Zika Virus Isolates Induce Premature Differentiation of Neural Progenitors in Human Brain Organoids. Cell Stem Cell *20*, 397–406.e5.

Garcez, P.P., Loiola, E.C., Madeiro da Costa, R., Higa, L.M., Trindade, P., Delvecchio, R., Nascimento, J.M., Brindeiro, R., Tanuri, A., and Rehen, S.K. (2016). Zika virus impairs growth in human neurospheres and brain organoids. Science *352*, 816–818.

Giraldo, D., Wilcox, D.R., and Longnecker, R. (2020). The Innate Immune Response to Herpes Simplex Virus 1 Infection Is Dampened in the Newborn Brain and Can Be Modulated by Exogenous Interferon Beta To Improve Survival. mBio *11*, e00921-20.

Gladwyn-Ng, I., Cordón-Barris, L., Alfano, C., Creppe, C., Couderc, T., Morelli, G., Thelen, N., America, M., Bessières, B., Encha-Razavi, F., et al. (2018). Stress-induced unfolded protein response contributes to Zika virus-associated microcephaly. Nat. Neurosci. *21*, 63–71.

Gobillot, T.A., Humes, D., Sharma, A., Kikawa, C., and Overbaugh, J. (2020). The Robust Restriction of Zika Virus by Type-I Interferon in A549 Cells Varies by Viral Lineage and Is Not Determined by IFITM3. Viruses *12*, 503.

Gorman, M.J., Caine, E.A., Zaitsev, K., Begley, M.C., Weger-Lucarelli, J., Uccellini, M.B., Tripathi, S., Morrison, J., Yount, B.L., Dinnon, K.H., 3rd, et al. (2018). An Immunocompetent Mouse Model of Zika Virus Infection. Cell Host Microbe *23*, 672–685.e6.

Gottfried, C., Bambini-Junior, V., Francis, F., Riesgo, R., and Savino, W. (2015). The Impact of Neuroimmune Alterations in Autism Spectrum Disorder. Front. Psychiatry *6*, 121.

Grant, A., Ponia, S.S., Tripathi, S., Balasubramaniam, V., Miorin, L., Sourisseau, M., Schwarz, M.C., Sánchez-Seco, M.P., Evans, M.J., Best, S.M., and García-Sastre, A. (2016). Zika Virus Targets Human STAT2 to Inhibit Type I Interferon Signaling. Cell Host Microbe *19*, 882–890.

Hamel, R., Dejarnac, O., Wichit, S., Ekchariyawat, P., Neyret, A., Luplertlop, N., Perera-Lecoin, M., Surasombatpattana, P., Talignani, L., Thomas, F., et al. (2015). Biology of Zika Virus Infection in Human Skin Cells. J. Virol. *89*, 8880–8896.

Hanners, N.W., Eitson, J.L., Usui, N., Richardson, R.B., Wexler, E.M., Konopka, G., and Schoggins, J.W. (2016). Western Zika Virus in Human Fetal Neural Progenitors Persists Long Term with Partial Cytopathic and Limited Immunogenic Effects. Cell Rep. *15*, 2315–2322.

Härle, P., Lauret, E., Pitha, P.M., De Maeyer, E., and Carr, D.J. (2001). Expression of human and macaque type I IFN transgenes interferes with HSV-1 replication at the transcriptional and translational levels: IFN-beta is more potent than IFN-alpha 2. Virology *290*, 237–248.

Härle, P., Cull, V., Guo, L., Papin, J., Lawson, C., and Carr, D.J.J. (2002). Transient transfection of mouse fibroblasts with type I interferon transgenes provides various degrees of protection against herpes simplex virus infection. Antiviral Res. *56*, 39–49.

Hatakeyama, J., Wakamatsu, Y., Nagafuchi, A., Kageyama, R., Shigemoto, R., and Shimamura, K. (2014). Cadherin-based adhesions in the apical endfoot are required for active Notch signaling to control neurogenesis in vertebrates. Development *141*, 1671–1682.

He, B., Gross, M., and Roizman, B. (1997). The gamma(1)34.5 protein of herpes simplex virus 1 complexes with protein phosphatase 1alpha to dephosphorylate the alpha subunit of the eukaryotic translation initiation factor 2 and preclude the shutoff of protein synthesis by double-stranded RNA-activated protein kinase. Proc. Natl. Acad. Sci. USA *94*, 843–848.

Heinz, S., Benner, C., Spann, N., Bertolino, E., Lin, Y.C., Laslo, P., Cheng, J.X., Murre, C., Singh, H., and Glass, C.K. (2010). Simple combinations of lineage-determining transcription factors prime cis-regulatory elements required for macrophage and B cell identities. Mol. Cell *38*, 576–589.

Hensel, N., Raker, V., Förthmann, B., Detering, N.T., Kubinski, S., Buch, A., Katzilieris-Petras, G., Spanier, J., Gudi, V., Wagenknecht, S., et al. (2019). HSV-1 triggers paracrine fibroblast growth factor response from cortical brain cells via immediate-early protein ICP0. J. Neuroinflammation *16*, 248.

Herber, S., Silva, A.A., Sanseverino, M.T.V., Friedrich, L., Ranieri, T.M.S., Favreto, C., Fraga, L.R., Terra, A.P., Schwartz, I.V.D., and Schuler-Faccini, L. (2019). Prevalence and causes of congenital microcephaly in the absence of a Zika virus outbreak in southern Brazil. J. Pediatr. (Rio J.) *95*, 600–606.

Herring, J.A., Elison, W.S., and Tessem, J.S. (2019). Function of Nr4a Orphan Nuclear Receptors in Proliferation, Apoptosis and Fuel Utilization Across Tissues. Cells *8*, 1373.

Hess, J., Angel, P., and Schorpp-Kistner, M. (2004). AP-1 subunits: quarrel and harmony among siblings. J. Cell Sci. *117*, 5965–5973.

Honda, K., and Taniguchi, T. (2006). IRFs: master regulators of signalling by Toll-like receptors and cytosolic pattern-recognition receptors. Nat. Rev. Immunol. *6*, 644–658.

Honein, M.A., Dawson, A.L., Petersen, E.E., Jones, A.M., Lee, E.H., Yazdy, M.M., Ahmad, N., Macdonald, J., Evert, N., Bingham, A., et al.; US Zika Pregnancy Registry Collaboration (2017). Birth Defects Among Fetuses and Infants of US Women With Evidence of Possible Zika Virus Infection During Pregnancy. JAMA *317*, 59–68.

Hu, B., Li, X., Huo, Y., Yu, Y., Zhang, Q., Chen, G., Zhang, Y., Fraser, N.W., Wu, D., and Zhou, J. (2016). Cellular responses to HSV-1 infection are linked to specific types of alterations in the host transcriptome. Sci. Rep. *6*, 28075.

Hummer, B.T., Li, X.L., and Hassel, B.A. (2001). Role for p53 in gene induction by double-stranded RNA. J. Virol. *75*, 7774–7777.

Ivashkiv, L.B., and Donlin, L.T. (2014). Regulation of type I interferon responses. Nat. Rev. Immunol. *14*, 36–49.

Kadowaki, M., Nakamura, S., Machon, O., Krauss, S., Radice, G.L., and Takeichi, M. (2007). N-cadherin mediates cortical organization in the mouse brain. Dev. Biol. *304*, 22–33.

Kanton, S., Boyle, M.J., He, Z., Santel, M., Weigert, A., Sanchís-Calleja, F., Guijarro, P., Sidow, L., Fleck, J.S., Han, D., et al. (2019). Organoid single-cell genomic atlas uncovers human-specific features of brain development. Nature *574*, 418–422.

Kasmapour, B., Kubsch, T., Rand, U., Eiz-Vesper, B., Messerle, M., Vondran, F.W.R., Wiegmann, B., Haverich, A., and Cicin-Sain, L. (2017). Myeloid Dendritic Cells Repress Human Cytomegalovirus Gene Expression and Spread by Releasing Interferon-Unrelated Soluble Antiviral Factors. J. Virol. *92*, 795.

Kaur, B., Chiocca, E.A., and Cripe, T.P. (2012). Oncolytic HSV-1 virotherapy: clinical experience and opportunities for progress. Curr. Pharm. Biotechnol. *13*, 1842–1851.

Keenan, A.B., Torre, D., Lachmann, A., Leong, A.K., Wojciechowicz, M.L., Utti, V., Jagodnik, K.M., Kropiwnicki, E., Wang, Z., and Ma'ayan, A. (2019). ChEA3: transcription factor enrichment analysis by orthogonal omics integration. Nucleic Acids Res. *47* (W1), W212–W224.

Keniry, M., Dearth, R.K., Persans, M., and Parsons, R. (2014). New Frontiers for the NFIL3 bZIP Transcription Factor in Cancer, Metabolism and Beyond. Discoveries (Craiova) *2*, e15.

Kim, D., Pertea, G., Trapnell, C., Pimentel, H., Kelley, R., and Salzberg, S.L. (2013). TopHat2: accurate alignment of transcriptomes in the presence of insertions, deletions and gene fusions. Genome Biol. *14*, R36.

Kim, J., Koo, B.-K., and Yoon, K.-J. (2019). Modeling Host-Virus Interactions in Viral Infectious Diseases Using Stem-Cell-Derived Systems and CRISPR/Cas9 Technology. Viruses *11*, 124.

Krummenacher, C., Baribaud, I., Eisenberg, R.J., and Cohen, G.H. (2003). Cellular localization of nectin-1 and glycoprotein D during herpes simplex virus infection. J. Virol. *77*, 8985–8999.

Kumar, A., Hou, S., Airo, A.M., Limonta, D., Mancinelli, V., Branton, W., Power, C., and Hobman, T.C. (2016). Zika virus inhibits type-I interferon production and downstream signaling. EMBO Rep. *17*, 1766–1775.

Lafaille, F.G., Pessach, I.M., Zhang, S.-Y., Ciancanelli, M.J., Herman, M., Abhyankar, A., Ying, S.-W., Keros, S., Goldstein, P.A., Mostoslavsky, G., et al. (2012). Impaired intrinsic immunity to HSV-1 in human iPSC-derived TLR3-deficient CNS cells. Nature *491*, 769–773.

Lancaster, M.A., and Knoblich, J.A. (2014). Generation of cerebral organoids from human pluripotent stem cells. Nat. Protoc. *9*, 2329–2340.

Lancaster, M.A., Renner, M., Martin, C.-A., Wenzel, D., Bicknell, L.S., Hurles, M.E., Homfray, T., Penninger, J.M., Jackson, A.P., and Knoblich, J.A. (2013). Cerebral organoids model human brain development and microcephaly. Nature *501*, 373–379.

Lanciotti, R.S., Kosoy, O.L., Laven, J.J., Velez, J.O., Lambert, A.J., Johnson, A.J., Stanfield, S.M., and Duffy, M.R. (2008). Genetic and serologic properties of Zika virus associated with an epidemic, Yap State, Micronesia, 2007. Emerg. Infect. Dis. *14*, 1232–1239.

Langmead, B., and Salzberg, S.L. (2012). Fast gapped-read alignment with Bowtie 2. Nat. Methods *9*, 357–359.

Leib, D.A., Harrison, T.E., Laslo, K.M., Machalek, M.A., Moorman, N.J., and Virgin, H.W. (1999). Interferons regulate the phenotype of wild-type and mutant herpes simplex viruses in vivo. J. Exp. Med. *189*, 663–672.

Li, H., and Durbin, R. (2009). Fast and accurate short read alignment with Burrows-Wheeler transform. Bioinformatics *25*, 1754–1760.

Li, R.Y., and Tsutsui, Y. (2000). Growth retardation and microcephaly induced in mice by placental infection with murine cytomegalovirus. Teratology *62*, 79–85.

Li, C., Xu, D., Ye, Q., Hong, S., Jiang, Y., Liu, X., Zhang, N., Shi, L., Qin, C.-F., and Xu, Z. (2016). Zika Virus Disrupts Neural Progenitor Development and Leads to Microcephaly in Mice. Cell Stem Cell *19*, 120–126.

Li, C., Deng, Y.-Q., Wang, S., Ma, F., Aliyari, R., Huang, X.-Y., Zhang, N.-N., Watanabe, M., Dong, H.-L., Liu, P., et al. (2017). 25-Hydroxycholesterol Protects Host against Zika Virus Infection and Its Associated Microcephaly in a Mouse Model. Immunity *46*, 446–456.

Li, S.-F., Gong, M.-J., Zhao, F.-R., Shao, J.-J., Xie, Y.-L., Zhang, Y.-G., and Chang, H.-Y. (2018). Type I Interferons: Distinct Biological Activities and Current Applications for Viral Infection. Cell. Physiol. Biochem. *51*, 2377–2396.

Lima, M.C., de Mendonça, L.R., Rezende, A.M., Carrera, R.M., Aníbal-Silva, C.E., Demers, M., D'Aiuto, L., Wood, J., Chowdari, K.V., Griffiths, M., et al. (2019). The Transcriptional and Protein Profile From Human Infected Neuroprogenitor Cells Is Strongly Correlated to Zika Virus Microcephaly Cytokines Phenotype Evidencing a Persistent Inflammation in the CNS. Front. Immunol. *10*, 1928.

Lin, J.-Y., Kuo, R.-L., and Huang, H.-I. (2019). Activation of type I interferon antiviral response in human neural stem cells. Stem Cell Res. Ther. *10*, 387.

Liu, L., Chen, Z., Zhang, X., Li, S., Hui, Y., Feng, H., Du, Y., Jin, G., Zhou, X., and Zhang, X. (2019). Protection of ZIKV infection-induced neuropathy by abrogation of acute antiviral response in human neural progenitors. Cell Death Differ. *26*, 2607–2621.

Looker, K.J., Magaret, A.S., May, M.T., Turner, K.M.E., Vickerman, P., Newman, L.M., and Gottlieb, S.L. (2017). First estimates of the global and

regional incidence of neonatal herpes infection. Lancet Glob. Health *5*, e300–e309.

Love, M.I., Huber, W., and Anders, S. (2014). Moderated estimation of fold change and dispersion for RNA-seq data with DESeq2. Genome Biol. *15*, 550.

Marquez, L., Levy, M.L., Munoz, F.M., and Palazzi, D.L. (2011). A report of three cases and review of intrauterine herpes simplex virus infection. Pediatr. Infect. Dis. J. *30*, 153–157.

Marsico, C., and Kimberlin, D.W. (2017). Congenital Cytomegalovirus infection: advances and challenges in diagnosis, prevention and treatment. Ital. J. Pediatr. *43*, 38.

Mi, H., Muruganujan, A., Casagrande, J.T., and Thomas, P.D. (2013). Large-scale gene function analysis with the PANTHER classification system. Nat. Protoc. *8*, 1551–1566.

Miller, J.A., Ding, S.-L., Sunkin, S.M., Smith, K.A., Ng, L., Szafer, A., Ebbert, A., Riley, Z.L., Royall, J.J., Aiona, K., et al. (2014). Transcriptional landscape of the prenatal human brain. Nature *508*, 199–206.

Ming, G.-L., Tang, H., and Song, H. (2016). Advances in Zika Virus Research: Stem Cell Models, Challenges, and Opportunities. Cell Stem Cell *19*, 690–702.

Mlakar, J., Korva, M., Tul, N., Popović, M., Poljšak-Prijatelj, M., Mraz, J., Kolenc, M., Resman Rus, K., Vesnaver Vipotnik, T., Fabjan Vodušek, V., et al. (2016). Zika Virus Associated with Microcephaly. N. Engl. J. Med. *374*, 951–958.

Nepusz, T., Yu, H., and Paccanaro, A. (2012). Detecting overlapping protein complexes in protein-protein interaction networks. Nat. Methods *9*, 471–472.

Ng, C.T., Mendoza, J.L., Garcia, K.C., and Oldstone, M.B.A. (2016). Alpha and Beta Type 1 Interferon Signaling: Passage for Diverse Biologic Outcomes. Cell *164*, 349–352.

Paijo, J., Döring, M., Spanier, J., Grabski, E., Nooruzzaman, M., Schmidt, T., Witte, G., Messerle, M., Hornung, V., Kaever, V., and Kalinke, U. (2016). cGAS Senses Human Cytomegalovirus and Induces Type I Interferon Responses in Human Monocyte-Derived Cells. PLoS Pathog. *12*, e1005546.

Qi, Y., Zhang, X.-J., Renier, N., Wu, Z., Atkin, T., Sun, Z., Ozair, M.Z., Tchieu, J., Zimmer, B., Fattahi, F., et al. (2017). Combined small-molecule inhibition accelerates the derivation of functional cortical neurons from human pluripotent stem cells. Nat. Biotechnol. *35*, 154–163.

Qian, X., Nguyen, H.N., Song, M.M., Hadiono, C., Ogden, S.C., Hammack, C., Yao, B., Hamersky, G.R., Jacob, F., Zhong, C., et al. (2016). Brain-Region-Specific Organoids Using Mini-bioreactors for Modeling ZIKV Exposure. Cell *165*, 1238–1254.

Qiao, H., Guo, M., Shang, J., Zhao, W., Wang, Z., Liu, N., Li, B., Zhou, Y., Wu, Y., and Chen, P. (2020). Herpes simplex virus type 1 infection leads to neurodevelopmental disorder-associated neuropathological changes. PLoS Pathog. *16*, e1008899.

Reiss, K., Maretzky, T., Ludwig, A., Tousseyn, T., de Strooper, B., Hartmann, D., and Saftig, P. (2005). ADAM10 cleavage of N-cadherin and regulation of cell-cell adhesion and beta-catenin nuclear signalling. EMBO J. *24*, 742–752.

Richart, S.M., Simpson, S.A., Krummenacher, C., Whitbeck, J.C., Pizer, L.I., Cohen, G.H., Eisenberg, R.J., and Wilcox, C.L. (2003). Entry of herpes simplex virus type 1 into primary sensory neurons in vitro is mediated by Nectin-1/HveC. J. Virol. *77*, 3307–3311.

Rios, A.C., and Clevers, H. (2018). Imaging organoids: a bright future ahead. Nat. Methods *15*, 24–26.

Ritchie, M.E., Phipson, B., Wu, D., Hu, Y., Law, C.W., Shi, W., and Smyth, G.K. (2015). limma powers differential expression analyses for RNA-sequencing and microarray studies. Nucleic Acids Res. *43*, e47.

Rousso, D.L., Pearson, C.A., Gaber, Z.B., Miquelajauregui, A., Li, S., Portera-Cailliau, C., Morrisey, E.E., and Novitch, B.G. (2012). Foxp-mediated suppression of N-cadherin regulates neuroepithelial character and progenitor maintenance in the CNS. Neuron *74*, 314–330.

Sandler, N.G., Bosinger, S.E., Estes, J.D., Zhu, R.T.R., Tharp, G.K., Boritz, E., Levin, D., Wijeyesinghe, S., Makamdop, K.N., del Prete, G.Q., et al. (2014). Type I interferon responses in rhesus macaques prevent SIV infection and slow disease progression. Nature *511*, 601–605.

Schneider, W.M., Chevillotte, M.D., and Rice, C.M. (2014). Interferon-stimulated genes: a complex web of host defenses. Annu. Rev. Immunol. *32*, 513–545.

Schwartz, D.A. (2017). The Origins and Emergence of Zika Virus, the Newest TORCH Infection: What's Old Is New Again. Arch. Pathol. Lab. Med. *141*, 18–25.

Scuderi, S., Altobelli, G.G., Cimini, V., Coppola, G., and Vaccarino, F.M. (2021). Cell-to-Cell Adhesion and Neurogenesis in Human Cortical Development: A Study Comparing 2D Monolayers with 3D Organoid Cultures. Stem Cell Reports *16*, 264–280.

Simões-Costa, M., and Bronner, M.E. (2015). Establishing neural crest identity: a gene regulatory recipe. Development *142*, 242–257.

Simonin, Y., Loustalot, F., Desmetz, C., Foulongne, V., Constant, O., Fournier-Wirth, C., Leon, F., Molès, J.-P., Goubaud, A., Lemaitre, J.-M., et al. (2016). Zika Virus Strains Potentially Display Different Infectious Profiles in Human Neural Cells. EBioMedicine *12*, 161–169.

Simpson, S.A., Manchak, M.D., Hager, E.J., Krummenacher, C., Whitbeck, J.C., Levin, M.J., Freed, C.R., Wilcox, C.L., Cohen, G.H., Eisenberg, R.J., and Pizer, L.I. (2005). Nectin-1/HveC Mediates herpes simplex virus type 1 entry into primary human sensory neurons and fibroblasts. J. Neurovirol. *11*, 208–218.

Sison, S.L., O'Brien, B.S., Johnson, A.J., Seminary, E.R., Terhune, S.S., and Ebert, A.D. (2019). Human Cytomegalovirus Disruption of Calcium Signaling in Neural Progenitor Cells and Organoids. J. Virol. *93*, e00954-19.

Sorgeloos, F., Kreit, M., Hermant, P., Lardinois, C., and Michiels, T. (2013). Antiviral type I and type III interferon responses in the central nervous system. Viruses *5*, 834–857.

Souza, B.S.F., Sampaio, G.L.A., Pereira, C.S., Campos, G.S., Sardi, S.I., Freitas, L.A.R., Figueira, C.P., Paredes, B.D., Nonaka, C.K.V., Azevedo, C.M., et al. (2016). Zika virus infection induces mitosis abnormalities and apoptotic cell death of human neural progenitor cells. Sci. Rep. *6*, 39775.

Sun, G., Chiuppesi, F., Chen, X., Wang, C., Tian, E., Nguyen, J., Kha, M., Trinh, D., Zhang, H., Marchetto, M.C., et al. (2020). Modeling Human Cytomegalovirus-Induced Microcephaly in Human iPSC-Derived Brain Organoids. Cell Rep. Med. *1*, 100002.

Suzuki, R., and Shimodaira, H. (2006). Pvclust: an R package for assessing the uncertainty in hierarchical clustering. Bioinformatics *22*, 1540–1542.

Thiery, J.P., Acloque, H., Huang, R.Y.J., and Nieto, M.A. (2009). Epithelial-mesenchymal transitions in development and disease. Cell *139*, 871–890.

Wang, K., Mahalingam, G., Hoover, S.E., Mont, E.K., Holland, S.M., Cohen, J.I., and Straus, S.E. (2007). Diverse herpes simplex virus type 1 thymidine kinase mutants in individual human neurons and Ganglia. J. Virol. *81*, 6817–6826.

Wang, J.P., Bowen, G.N., Zhou, S., Cerny, A., Zacharia, A., Knipe, D.M., Finberg, R.W., and Kurt-Jones, E.A. (2012). Role of specific innate immune responses in herpes simplex virus infection of the central nervous system. J. Virol. *86*, 2273–2281.

Watanabe, Y., Someya, T., and Nawa, H. (2010). Cytokine hypothesis of schizophrenia pathogenesis: evidence from human studies and animal models. Psychiatry Clin. Neurosci. *64*, 217–230.

Watanabe, M., Buth, J.E., Vishlaghi, N., de la Torre-Ubieta, L., Taxidis, J., Khakh, B.S., Coppola, G., Pearson, C.A., Yamauchi, K., Gong, D., et al. (2017). Self-Organized Cerebral Organoids with Human-Specific Features Predict Effective Drugs to Combat Zika Virus Infection. Cell Rep. *21*, 517–532.

Zhang, F., Hammack, C., Ogden, S.C., Cheng, Y., Lee, E.M., Wen, Z., Qian, X., Nguyen, H.N., Li, Y., Yao, B., et al. (2016). Molecular signatures associated with ZIKV exposure in human cortical neural progenitors. Nucleic Acids Res. *44*, 8610–8620.

Zhao, M., Zhang, J., Phatnani, H., Scheu, S., and Maniatis, T. (2012). Stochastic expression of the interferon-β gene. PLoS Biol. *10*, e1001249.

Please cite this article in press as: Krenn et al., Organoid modeling of Zika and herpes simplex virus 1 infections reveals virus-specific responses leading to microcephaly, Cell Stem Cell (2021), https://doi.org/10.1016/j.stem.2021.03.004

CellPress

STAR★METHODS

KEY RESOURCES TABLE

REAGENT or RESOURCE	SOURCE	IDENTIFIER
Antibodies		
mouse anti-Flavivirus D1-4G2-4-15 (ZIKVA, 1:600)	Merck Millipore	Cat# MAB10216; RRID: AB_827205
rabbit anti-ZIKA virus Envelope protein (ZIKVE, 1:250)	Genetex	Cat# GTX133314; RRID: AB_2747413
rabbit anti-cleaved Caspase3 (1:500)	Cell Signaling	Cat# 9661S; RRID: AB_2341188
goat anti-Sox1 (1:200)	R&D Systems	Cat# AF3369; RRID: AB_2239879
rabbit anti-Sox2 (1:1000)	Abcam	Cat# ab97959; RRID: AB_2341193
goat anti-Sox2 (1:200)	R&D systems	Cat# AF2018; RRID: AB_355110
mouse anti- ICP4 10F1 (1:500)	Abcam	Cat# ab6514; RRID: AB_305537
rabbit anti-HSV1 (1:500)	Abcam	Cat# ab9533; RRID: AB_307320
rabbit anti-IRF3 (D6I4C) XP (1:500)	Cell Signaling	Cat# 11904; RRID: AB_2722521
mouse anti-STAT2 (1:100)	Santa Cruz Biotechnology	Cat# sc-1668; RRID: AB_628291
chicken anti-GFP (1:1000)	Aves laboratory	Cat# GFP-1020; RRID: AB_10000240
rabbit anti-tdTomato (1:500)	Clontech	Cat# 632496; RRID: AB_10013483
goat anti-tdTomato (1:200)	Sicgen	Cat# AB8181-200; RRID: AB_2722750
mouse anti-N-Cadherin (1:200)	BD	Cat# 610920; RRID: AB_2077527
rabbit anti-Nestin (1:1000)	Abcam	Cat# ab10538; RRID: AB_297279
sheep anti-Pax6 (1:200)	R&D systems	Cat# AF8150; RRID: AB_2827378
goat anti-SNAI1 (1:500)	Abcam	Cat# ab53519; RRID: AB_881666
rabbit anti-Beta 3 tubulin (1:750)	Covance	Cat# PRB-435P; RRID: AB_291637
mouse anti-mNeonGreen (1:200)	ChromoTek	Cat# 32f6-100; RRID: AB_2827566
Bacterial and virus strains		
French Polynesian ZIKA virus, strain H/PF/2013, clinical isolate	EVAg project	Cat# 001v-EVA1545
Herpes Simplex Virus 1 (HSV-1), strain F	Calistri et al., 2003	N/A
Herpes Simplex Virus 1 (HSV-1) R3616, strain F	Chou et al., 1990	N/A
Human Cytomegalovirus (HCMV) UL122/123-mNeonGreen, strain TB40/E	Kasmapour et al., 2017	N/A
Chemicals, peptides, and recombinant proteins		
mTeSR1 complete Kit	Stem Cell Technologies	Cat# 85875
Gelatin	Sigma-Aldrich	Cat# G1890; CAS: 9000-70-8
CF-1-γ-irradiated mouse embryonic fibroblasts	Global Stem	Cat# GSC-6001G
Matrigel® Basement Membrane Matrix	Corning	Cat# 356235
hESC-qualified Matrigel	Corning	Cat# 354277
bFGF	Peprotech	Cat# 100-18B
Y-27632 Rock Inhibitor	Selleck Chemicals	Cat# S1049; CAS: 129830-38-2
Ultra-low attachment 96-well plates	Corning	Cat# COR7007
N2 supplement	Thermo Fischer Scientific	Cat# 17502048; CAS: 17502-048
B27 supplement – Vitamin A	Thermo Fischer Scientific	Cat# 12587010; CAS: 12587010
B27 supplement	Thermo Fischer Scientific	Cat# 17504044; CAS: 17504-044
Beta-mercaptoethanol (BME)	Merck Millipore	Cat# 805740; CAS: 60-24-2
Human Insulin solution	Sigma-Aldrich	Cat# I9278; CAS: 11061-68-0
Heparin sodium salt	Sigma-Aldrich	Cat# H3149; CAS: 9041-08-1
Accutase	Sigma-Aldrich	Cat# A6964
Collagenase type IV	Life Technologies	Cat# 17104019; CAS: 17-104-019

(*Continued on next page*)

Please cite this article in press as: Krenn et al., Organoid modeling of Zika and herpes simplex virus 1 infections reveals virus-specific responses leading to microcephaly, Cell Stem Cell (2021), https://doi.org/10.1016/j.stem.2021.03.004

Continued

REAGENT or RESOURCE	SOURCE	IDENTIFIER
Dispase	Invitrogen	Cat# 17105-041; CAS: 42613-33-2
KnockOut Serum Replacement (KOSR)	Thermo Fisher Scientific	Cat# 10828028; CAS: 10828-028
0.05% Trypsin/EDTA solution	Thermo Fisher Scientific	Cat# 15400054; CAS: 15-400-054
GlutaMAX 100X	Thermo Fisher Scientific	Cat# 35050-038
MEM-NEEA Solution 100X	Sigma-Aldrich	Cat# M7145
DMEM-F12	GIBCO	Cat# 11330-057
Neurobasal medium	GIBCO	Cat# 21103049
BDNF	Stem Cell Technologies	Cat# 78005.3; CAS: 78005
GDNF	Stem Cell Technologies	Cat# 78058.3; CAS: 78058
db-cAMP	MedChem Express	Cat# HY-B0764; CAS: 16980-89-5
Essential 6 medium	Thermo Fisher Scientific	Cat# A1516401
Poly-L-ornithine hydrobromide	Sigma-Aldrich	Cat# P3655; CAS: 27378-49-0
Laminin	Sigma-Aldrich	Cat# L2020; CAS: 114956-81-9
LDN193189	Sigma-Aldrich	Cat# SML0559; CAS: 1062368-24-4
SB431542	Stemgent	Cat# 04-0010-10; CAS:381836-41-9
XAV939	Abcam	Cat# ab120897; CAS: 284028-89-3
SU5402	Sigma-Aldrich	Cat# SML0443; CAS: 215543-92-3
DAPT	Tocris	Cat# 2634; CAS: 208255-80
DPBS, no calcium, no magnesium	GIBCO	Cat# 14190-169
DPBS, calcium, magnesium	Thermo Fischer Scientific	Cat# 14040-174
Penicillin/Streptomycin	Sigma-Aldrich	Cat# P0781; CAS: 4744-08-5
EDTA solution	Sigma-Aldrich	Cat# E8008; CAS: 60-00-4
Puromycin	Jena Bioscience	Cat# NU-931-5; CAS: 1416561-90-4
G418	Invivogen	Cat# ant-gn-1; CAS: 108321-42-2
QuickExtract DNA Extraction Solution	EpiCentre	Cat# QE09050
Cell Recovery Solution	Corning	Cat# 354253
SuperScript III	ThermoFisher	Cat# 18080051; CAS: 18080-051
Human Recombinant IFNα2	Peprotech	Cat# 300-02AA
Human Recombinant IFNβ	Peprotech	Cat# 300-02BC
Human Recombinant IFNλ1	Peprotech	Cat# 300-02K
Human Recombinant IFNλ2	Peprotech	Cat# 300-02L
Bovine Serum Albumin (BSA)	Sigma-Aldrich	Cat# A7030; CAS: 9048-46-8
poly(I:C)-LMW	Invivogen	Cat# tlrl-picw; CAS: 31852-29-6
Lipofectamine 3000 Transfection reagent	Thermo Fisher Scientific	Cat# L3000001; CAS: L3000-001
Sucrose	Sigma-Aldrich	Cat# 84097; CAS: 57-50-1
Normal Donkey Serum	EMD Millipore	Cat# S30-M
Paraformaldehyde	Sigma-Aldrich	Cat# 441244; CAS: 30525-89-4
DAPI	Sigma-Aldrich	Cat# D9542; CAS: 28718-90-3
Fluorescent mounting medium	Dako	Cat# S3023
Random Hexamers	Thermo Fisher Scientific	Cat# N8080127
Critical commercial assays		
Rneasy Micro Kit	QIAGEN	Cat# 74004
Rnase-Free Dnase set	QIAGEN	Cat# 79254
NEBNext Poly(A) mRNA Magnetic Isolation Module	New England Biolabs	Cat# E7490L
GoTaq qPCR master mix	Promega	Cat# A6002
Stem Cell Nucleofector Kit 1	Lonza	Cat# VPH-5012
Purelink Viral RNA/DNA Mini Kit	Thermo Fisher Scientific	Cat# 12280050
GoTaq polymerase	Promega	Cat# M7823
KOD Xtreme Hot Start DNA polymerase	Merck Millipore	Cat# US171975-3

(*Continued on next page*)

Please cite this article in press as: Krenn et al., Organoid modeling of Zika and herpes simplex virus 1 infections reveals virus-specific responses leading to microcephaly, Cell Stem Cell (2021), https://doi.org/10.1016/j.stem.2021.03.004

Continued

REAGENT or RESOURCE	SOURCE	IDENTIFIER
VeriKine-HS Human IFN-α All Subtype TCM ELISA Kit	PBL Assay Science	Cat# 41135-1
VeriKine-HS Human IFN Beta TCM ELISA, High Sensitivity	PBL Assay Science	Cat# 41435-1
Deposited data		
RNA-seq data of MOCK- and ZIKV- infected brain organoids and upon interferon treatment	This study	GEO: GSE123816
RNA-seq data of MOCK- and HSV- infected brain organoids and upon interferon treatment	This study	GEO: GSE145496
Experimental models: cell lines		
Human: WT hESCs H9	WiCell	W0A9
Human: hESCs H9 carrying *IFNB1>GFP* and *ISRE>tdTomato* cassettes in the AAVS1 locus	This study	N/A
Human: A549 cells	ATCC	CCL-185
Monkey: Vero cells	ATCC	CCL-81
Oligonucleotides		
Primers for RT-qPCR, see Table S4	This study	N/A
Primer ICP34.5 Forward 5- > 3: CTGCACGCACATGCTTGCCT	(Bower et al., 1999)	N/A
Primer ICP34.5 Reverse 5- > 3: CTCGGGTGTAACGTTAGACC	(Bower et al., 1999)	N/A
Primer TK Forward 5- > 3 tkF51: GAAACTCCCGCACCTCTTCGG	(Wang et al., 2007)	N/A
Primer TK Reverse 5- > 3 tkR61: GGTTCCTTCCGGTATTGTCTCC	(Wang et al., 2007)	N/A
Recombinant DNA		
AASV1 SA2APuro-2xCHS4-IFNB1 > eGFP-WPRE-SV40pA-2xCHS4 plasmid donor	This study	N/A
AAVS1 SA2ANeo-2xCHS4-ISRE > tdTomato-WPRE-SV40pA-2xCHS4 plasmid donor	This study	N/A
Software and algorithms		
Zeiss Zen (Blue edition)	Zeiss	https://www.zeiss.com/microscopy/int/products/microscope-software/zen-lite.html
ImageJ Fiji (2.0.0)	NIH	https://imagej.net/Fiji
GraphPad Prism 8.0	GraphPad	https://www.graphpad.com/scientific-software/prism/
Microsoft Excel	Microsoft	https://www.microsoft.com/de-at/microsoft-365/excel
Adobe Illustrator	Adobe	https://www.adobe.com/at/products/illustrator.html
TopHat (v2.1.1)	Johns Hopkins University	https://ccb.jhu.edu/software/tophat/index.shtml
Cytoscape	The Cytoscape Consortium	https://cytoscape.org/
FlowJo	BD Life Sciences	https://www.flowjo.com/

RESOURCE AVAILABILITY

Lead contact

Information and requests regarding reagents and biological materials should be addressed to the lead contact, Dr. Jürgen Knoblich (juergen.knoblich@imba.oeaw.ac.at).

Materials availability

All unique reagents and biological materials generated in this study are available from the lead contact, Dr. Jürgen Knoblich (juergen.knoblich@imba.oeaw.ac.at), in compliance with Material Transfer Agreements (MTA).

Please cite this article in press as: Krenn et al., Organoid modeling of Zika and herpes simplex virus 1 infections reveals virus-specific responses leading to microcephaly, Cell Stem Cell (2021), https://doi.org/10.1016/j.stem.2021.03.004

Data and code availability

RNA-seq data generated in this study have been deposited at NCBI Gene Expression Omnibus (GEO) under the accession numbers GEO: GSE123816 and GEO: GSE145496. The data that support the findings of this study are available from the Lead contact Dr. Jürgen Knoblich (juergen.knoblich@imba.oeaw.ac.at) upon reasonable request.

EXPERIMENTAL MODEL AND SUBJECT DETAILS

Human embryonic stem cells and cell lines

Human embryonic stem cells (hESCs) H9 were obtained from WiCell. Human lung epithelial carcinoma A549 cells and African green monkey kidney Vero cells were obtained from ATCC and maintained in regular Dulbecco's minimal essential medium (DMEM) supplemented with 10% fetal bovine serum (FBS) and 2 mM L-Glutamine. All cells were authenticated using a short tandem repeat (STR) assay. All cells were maintained in a 5% CO_2 incubator at 37°C and routinely tested for mycoplasma.

Viruses

The French Polynesian ZIKA virus strain (ZIKV, H/PF/2013) was propagated in Vero cells. Briefly, Vero cells were infected with ZIKV at multiplicity of infection (MOI) 0.1 and incubated at 37°C in a 5% CO_2 incubator. At 3 days post-infection, cell supernatants from infected cells were harvested and purified by centrifugation at 1500 rpm for 10 min to remove cellular debris. The viral titer was determined by tissue culture infective dose (TCID) assay performed on Vero cells. Briefly, confluent Vero cells plated in 96-well plates were infected with serially diluted ZIKV stocks and incubated at 37°C in a 5% CO_2 incubator. The assay was carried out in eight parallels wells for each dilution with the last column of 96-well plate as control cells without virus. At 5 days post-infection, the appearance of cytopathic effect (CPE) was examined by microscopy. The $TCID_{50}$ was calculated from the CPE induced in the cell culture. The wild-type Herpes Simplex Virus 1 (wt HSV-1, strain F) and the R3616 mutant HSV-1 virus (HSV-1 R3616, strain F) were generated previously (Chou et al., 1990) and kindly provided by B. Roizman (University of Chicago, Chicago, IL). HSV-1 viruses were grown and subjected to titer determination by plaque assay on Vero cell monolayers as previously described (Calistri et al., 2003). Human Cytomegalovirus (HCMV, strain TB40/E) expressing mNeonGreen fluorescence protein under the control of the endogenous HCMV major immediate-early (MIE) promoter of UL122/123 genes (HCMV-UL122/123-mNeonGreen) was generated and kindly provided by L. Cicin-Sain (Helmholtz Centre of Infection Research; Kasmapour et al., 2017). Note that this modified virus shows similar growth kinetics to the parental strain (Kasmapour et al., 2017). Viral stocks were aliquoted and stored at −80°C. Supernatants from uninfected Vero cells were prepared as performed during viral propagation and used as MOCK controls. Infection experiments were conducted under Biosafety Level 2 Plus containment.

METHOD DETAILS

Maintenance of hESCs

H9 cells were cultured under feeder-free or feeder-dependent conditions. Feeder-free H9 cells were seeded onto 6-well plates coated with hES-qualified matrigel and maintained in mTeSR1 medium. Cells were fed daily and passaged every 3-4 days using 0.5 mM EDTA solution treatment and mechanical dissociation. Feeder-dependent H9 cells were cultured on CF-1-γ-irradiated mouse embryonic fibroblasts seeded one day in advance onto gelatin-coated [0.1% (wt/vol) gelatin] 6-well plates. Cells were fed daily with stem cell medium containing DMEM-F12 supplemented with 20% KnockOut Serum Replacement, 3% FBS, 1X GlutaMAX, 1X minimum essential medium amino acids (MEM-NEAA), 0.1 mM beta-mercaptoethanol (BME), 20 ng/ml bFGF as previously described (Lancaster and Knoblich, 2014). Cells were passaged every 5-7 days following treatment with collagenase IV (0.1% wt/vol) for 15 minutes and mechanical dissociation.

Generation of interferon reporter lines

The reporter constructs were inserted into the AAVS1 safe-harbor locus of feeder-free H9 cells or A549 cells using TALEN technology as described before (Bagley et al., 2017). Donor plasmids were constructed to insert the following cassettes: (i) 2APuro-2xCHS4-IFNB1 > eGFP-WPRE-SV40-2xCHS4 and (ii) 2ANeo-2xCHS4-ISRE > tdTomato-WPRE-SV40-2xCHS4. Fragments spanning −1425 base pairs (bp) downstream and 40 bp upstream of the transcription start site of the human *IFNB1* gene and 353 bp downstream and 74 bp upstream of the transcription start site of the human *ISG15* gene (Hummer et al., 2001) were used as promoters. All donor plasmids were verified by sequencing. For reporter integration in H9 cells, 10^6 single cells prepared using accutase were nucleofected with the Amaxa nucleofector (Lonza) and Human Stem Cell Nucleofector Kit 1 solutions containing 0.5 μg of each of the TALEN plasmids and 1 μg of each of the two donor plasmids following manufacturer's guidelines. Nucleofected cells were grown for four days and then selected with 0.5 μg/ml puromycin and 100 μg/ml G418. For reporter integration in A549 cells, 1.2 x10^6 cells were seeded and one day later transfected with Lipofectamine 3000 and 1 μg of each of the TALEN plasmids and 1.5 μg of each donor plasmid following manufacturer's instructions. One day later, the medium was replaced and A549 cells were selected with 0.5 μg/ml puromycin and 750 μg/ml G418 starting from day 2. Surviving colonies of H9 and A549 cells were picked manually, transferred into 24-well plates and further expanded for genotyping and cryopreservation. For genotyping, DNA was extracted using the QuickExtract DNA Extraction Solution and a PCR assay was performed to identify correctly targeted AAVS1 insertions and loss of wild-type alleles in multiple clones. For *ISRE>tdTomato* expression analysis performed by flow cytometry (Figure S3C), organoids generated

from reporter cells (12-days-old) were incubated with recombinant interferons or vehicle. One day later, organoids were manually dissociated into single cells after 5 minutes of incubation with an accutase:trypsin (2:1 v/v) mix at room temperature. Single cell suspensions were diluted into 300 μl of culture medium and tdTomato expression was analyzed by flow cytometry on a LSRFortessa cell analyzer (BD Biosciences) using BD FACSDIVA software. Data were analyzed using FlowJo.

Generation of cerebral organoids

Cerebral organoids were generated as previously described (Lancaster et al., 2013; Lancaster and Knoblich, 2014). Briefly, on day 0 hESCs were dissociated into single cells by accutase treatment (feeder-free cells) or by collagenase IV/dispase treatment followed by a short treatment with trypsin (feeder-dependent cells). Cells were transferred to an ultra-low binding 96-well plate (9000 cells/well) containing stem cell medium supplemented with 4 ng/ml bFGF and 50 μM Rho-associated protein kinase (ROCK) inhibitor. On day 3, the medium was replaced with fresh stem cell medium. From day 5 or 6, the medium was replaced daily with Neural Induction Medium containing DMEM-F12 supplemented with 1X N2 supplement, 1ug/ml heparin solution, 1X GlutaMAX and 1X MEM-NEAA. On Day 10 or 11, organoids with visible neuroepithelia were embedded into droplets of Matrigel and transferred into 6-cm dishes in Expansion Medium consisting of 50% DMEM-F12, 50% Neurobasal medium, 1X N2, 1X B27 – Vitamin A, 2.5 μg/ml Insulin, 0.05 mM BME, 1X GlutaMAX, 1X MEM-NEAA and 1X Penicillin/Streptomycin. On day 15, media was replaced with Differentiation Medium consisting of 50% DMEM-F12, 50% Neurobasal medium, 1X N2, 1X B27, 2.5 μg/ml Insulin, 0.05mM BME, 1X GlutaMAX, 1X MEM-NEAA, 1X Penicillin/Streptomycin and organoids were cultured on an orbital shaker under 57 rpm rotating speed. The medium was changed every 2-3 days. From day 40 onward, organoids were fed with Differentiation Medium supplemented with 1% (v/v) matrigel basement membrane. From day 65 onward, organoids were fed with Differentiation Medium supplemented with BDNF (20 ng/ml), GDNF (20 ng/ml) and db-cAMP (1 mM). Organoids that passed the quality control criteria (Lancaster and Knoblich, 2014) were used. Criteria included visible surface brightening before embedding (as a proxy for an organized neuroepithelium) and formation of neural tube-like structures in matrigel.

Generation of 2D neural cultures

To generate dissociated 2D cultures of organoids (disOrganoids), 10-days-old organoids were plated onto matrigel-coated dishes in Neural Induction Medium. Three days later, plated organoids were incubated with accutase for 15 min at 37°C and manually dissociated into a single cell suspension. After a washing step, cells were resuspended in Neural Induction Medium supplemented with 10 μM ROCK inhibitor and plated as single cells onto matrigel-coated plates. One day later, the medium was replaced with Expansion Medium. Two days later (day 16), cells were dissociated again with accutase and plated onto matrigel-coated surfaces for further analysis. An outline of this protocol is presented in Figure S4A. To differentiate hESCs into hNPCs directly in 2D, we adapted a previously published protocol (Qi et al., 2017). Briefly, cells were dissociated with accutase and plated onto matrigel-coated plates at the density of 200,000 cells/cm^2 in mTeSR1 supplemented with 10 μM ROCK inhibitor. Differentiation was started the next day using E6 medium. Inhibitors used in LSB+X induction in E6 included LDN193189 (100 nM), SB431542 (10 μM) and XAV939 (2 μM) for treatment of 3 days. Then starting from day 3, LDN193189 (50 nM), SB431542 (5 μM), XAV939 (1 μM), SU5402 (2 μM) and DAPT (5 μM) were added to E6. On day 6, cells were dissociated by incubation with accutase at 37°C for 15 minutes, resuspended in E6 medium supplemented with 10 μM ROCK inhibitor and plated onto poly-L-ornithine (50 μg/ml) and laminin (5 μg/ml)-coated surfaces for further analysis. An outline of this protocol is shown in Figure S4I.

Infection of cerebral organoids

Organoid infection experiments were performed by adapting previous ZIKV infection paradigms (Dang et al., 2016; Gabriel et al., 2017). On day 10 or 11, organoids were incubated with a virus inoculum diluted in 200 μl of Neural induction Medium in ultra-low binding 96-well plates. An equivalent volume of MOCK medium was used for uninfected controls. Plates were incubated at 37°C in a 5% CO_2 incubator. One day later, organoids were embedded in Matrigel, transferred to 6-cm dishes in Expansion medium and cultured as described above. Details on the number of virus particles used in this study are provided in Tables S1 and S2. For infection at later stages, 40-days-old organoids were exposed to 600 PFU of HSV-1 diluted in Differentiation medium. One day later, the medium was replaced with fresh Differentiation medium containing 1% (v/v) matrigel basement membrane and cultured as described above. Supernatants were collected at 4, 8 or 12 dpi and frozen at −80°C. 125 μL of each supernatant was used to infect Vero cells in 12-well plates. Cells were fixed 24 hours post-infection and the level of infection was assessed by viral antigen expression using immunostaining.

Infection of 2D cultures

disOrganoids (day 17) were seeded onto glass coverslips in 12-well plates at a seeding density of 150000 cells/well. One day later, cells were incubated with 150000 $TCID_{50}$ units of ZIKV or with 187.5 PFU of HSV-1 for one day. For infection in A549 cells, 80000 cells were seeded onto a glass coverslip in 12-well plates. One day later, cells were incubated with 80000 $TCID_{50}$ units of ZIKV or with 50 PFU of HSV-1 for one day to match the infection doses used in organoids. An equivalent volume of MOCK medium was used for control conditions.

Interferon and poly(I:C) treatments

Recombinant human interferons were reconstituted at 10 μg/ml according to the manufacturer's instructions. Interferons were used at 10 ng/ml dose unless differently specified. Based on the biological activities provided by the manufacturer, 10 ng/ml dose of IFNα2

and IFNβ corresponds to activities of 1800 U/ml and 100 U/ml respectively. BSA solution (0.1%) was used as a vehicle for untreated conditions. For multiple-dose treatments, interferons or vehicle were freshly diluted into culture medium at 2, 4, 6 and 8 dpi. For poly(I:C) experiments, organoids (10-12 days-old) were transfected with 1 μg poly(I:C) diluted in 200 μl of Neural Induction Medium [corresponding to 5 μg/ml poly(I:C)] using Lipofectamine 3000 following manufacturer's instructions and incubated at 37°C in a 5% CO_2 humidified atmosphere for one day. For poly(I:C) treatment in 2D culture, cells were seeded onto glass coverslips in 12-well plates. One day later, cells were transfected with 25 ng/ml poly(I:C) using Lipofectamine 3000 Transfection Reagent. The medium was replaced after 6 hours and cells were further cultured at 37°C in a 5% CO_2 incubator for additional 18 hours. poly(I:C) was replaced with water in control transfections.

Cryo-sectioning, immunostaining and imaging

Organoids were fixed in 4% paraformaldehyde (PFA) overnight at 4°C. After extensive washes with PBS, organoids were immersed in 30% sucrose solution overnight, embedded in 10% gelatin solution and frozen. Samples were sectioned at 20 μm thickness using a cryostat (Leica). Organoid cryo-sections were fixed with 4% PFA for 10 minutes. After extensive washing with PBS, cryo-sections were permeabilized and blocked with blocking solution [10% normal donkey serum (NDS) containing 0.5% Triton X-100] for 45 min at room temperature. Sections were then incubated with primary antibodies diluted in antibody solution [10% normal donkey serum containing 0.1% Triton X-100] overnight at 4°C. After three washes of 10 min with PBS, sections were incubated with secondary antibodies diluted in antibody solution at room temperature for two hours and subsequently with DAPI solution (2 μg/ml) for 10 minutes. For immunostaining of 2D cultures, cells seeded on coverslips were fixed with 4% PFA for 30 minutes and washed extensively with PBS. Cells were permeabilized with PBS supplemented with 0.2% Triton X-100 for 5 min, washed with PBS and blocked with 10% NDS for one hour. Coverslips were then incubated with primary antibodies diluted in antibody solution for 2 hours at room temperature. Coverslips were washed with PBS and incubated with secondary antibodies for 45 minutes at room temperature, followed by incubation with DAPI solution for 3 minutes. Finally, both organoid sections and coverslips were washed three times with PBS containing 0.05% Triton X-100 and then mounted in fluorescent mounting medium. Primary antibodies used in this study and their dilutions are summarized in the KEY RESOURCES TABLE. Secondary antibodies AlexaFluor 488, 568 or 647 -conjugated donkey antibodies (Invitrogen) were used at 1:500 dilution. Immunostaining images were captured with Axio Imager confocal microscopes LSM700, 780 and 880 (Zeiss GmbH), using the "tile" and "stitching" functions in the Zen software when imaging large organoid areas. Immunostaining images of organoids in Figure 7 were acquired with an Axio Imager.Z2 microscope (Zeiss GmbH) equipped with an ORCA-Flash 4.0 V3 Digital CMOS Camera (Hamamatsu). Bright-field imaging of intact organoids was performed on a wide-field microscope (AxioVert.A1, Zeiss GmbH) with a SONY Chameleon®3 CM3-U3-31S4M CMOS camera (Zeiss GmbH). Images were converted into maximal intensity projections, adjusted for brightness levels and cropped (if used for magnified insets) using Fiji. Image quantifications were performed in Fiji.

Quantification of cytokine levels by ELISA

Levels of all IFNα species and IFNβ in organoid supernatants were measured using ELISA Kits according to manufacturer's instruction. Briefly, frozen supernatants from MOCK- and infected-organoids were thawed on ice and centrifuged at 13,000 rpm for 10 min to eliminate debris. Supernatants (3 mL for each sample) from three different experiments were concentrated using Centrifugal Filter Unit with Ultracel-3 membranes (UFC900308 Merck Millipore). For each sample (50 μl) absorbance at 450 nm and 540 nm were measured in duplicate using a microplate reader (Synergy H1 BioTek). Absorbance at 540 nm was subtracted from absorbance at 450 nm to correct for non-specific signals. Mean values of absorbance were multiplied for the concentration factor and used to estimate cytokine amounts (pg/ml) according to a standard curve of recombinant Human IFNα (0-125 pg/ml) or recombinant Human IFNβ (0-150 pg/ml).

RNA extraction and RT-qPCR analysis

For each condition and time point, 4–10 organoids were pooled into RNase-free tubes and chilled on ice. Organoids were washed with PBS and incubated with 1 mL of chilled Cell Recovery Solution for 1 hour on ice. Dissolved Matrigel was removed by rinsing twice in cold DEPC-treated PBS and samples were lysed in RLT buffer. RNA was extracted using the RNeasy Micro Kit and on-column DNase digestion was performed using RNase-Free DNase I following the manufacturer's protocol. cDNA synthesis was performed with SuperScript III and Random Hexamers using 500 ηg- 1 μg of total RNA according to the manufacturer's instructions. qPCR reactions were performed using GoTaq qPCR master mix on 384-well (CXF384) or 96-well (CXF96) BioRad machines using the following reaction protocol: (i) 95°C for 3 min, (ii) 95°C for 10 s, (iii) 62°C for 10 s, (iv) 72°C for 40 s, (v) go to 2, 40 cycles, (vi) 95°C for 1 min, and (vii) 50°C for 10 s. Quantification was performed in Excel by calculating the ΔCt value using TBP as a reference gene and the ΔΔCt value using age-matched untreated samples as calibrators. ACTIN was used as a reference gene in HSV-1 experiments. Data are presented as expression ($2^{-\Delta Ct}$) or fold change ($2^{-\Delta\Delta Ct}$). Primers used for RT-qPCR are provided in Table S4.

RNA-sequencing and analysis

For the ZIKV experiment, 3 replicates were used per condition and time point (4 and 12 dpi). For the HSV-1 experiment, 3 replicates were used per each condition and time point (4 and 8 days post-infection). Sample collection and RNA isolation were performed as described above. RNA concentration and quality were assessed with an RNA 6000 Nano Chip (Agilent Technologies). mRNA isolation was performed with NEBNext Poly(A) mRNA Magnetic Isolation Module. Barcoded samples were multiplexed and sequenced 50 bp

Please cite this article in press as: Krenn et al., Organoid modeling of Zika and herpes simplex virus 1 infections reveals virus-specific responses leading to microcephaly, Cell Stem Cell (2021), https://doi.org/10.1016/j.stem.2021.03.004

single-end on a HighSeq 2500 (Illumina). mRNA sample isolation, library preparation, and sequencing were done at the VBCF NGS Unit (https://www.vbcf.ac.at). Reads were screened for ribosomal RNA by aligning with BWA (v0.7.12) (Li and Durbin, 2009) against known rRNA sequences (RefSeq). rRNA-subtracted reads were aligned with TopHat (Kim et al., 2013) against the *Homo sapiens* genome (hg38). Microexon-search was enabled. Additionally, a gene model was provided as GTF (UCSC, 2015_01, hg38). rRNA loci were masked on the genome for downstream analysis. Aligned reads were counted with HTSeq (v0.6.1; intersection-nonempty) (Anders et al., 2015). The samples were subjected to differential expression analysis with DESeq2 (v1.16.1) (Love et al., 2014). Furthermore, reads were subjected to TPM estimation with Kallisto (v0.43.0) (Bray et al., 2016). Unless differently specified, analysis was performed on the DESeq2 datasets filtered for TPM values > 10, log2 Fold change absolute value of $\geq$ 1 and adjusted p value < 0.05. Gene Ontology (GO) enrichment analysis was performed with Gene Ontology Consortium using the PANTHER classification system (Mi et al., 2013). Highly connected clusters were identified with ClusterONE plug-in for Cytoscape (Nepusz et al., 2012). Transcription factor enrichment analysis was performed with ChEA3 (Keenan et al., 2019). Motif analysis was performed with HOMER Software v4.10 on promoter sequences of input genes from 500 bp upstream and 100 bp downstream of the transcription start site (Heinz et al., 2010). For the analysis shown in Figure 6J, reads were aligned to the HSV-1 strain F complete genome (GeneBank GU734771) with Bowtie2 (v2.2.9) (Langmead and Salzberg, 2012) and further processed as described above. For heatmaps shown in Figures 5 and 6, only the late time points were included in the analysis and processed for DESeq2 analysis as described above. Principal component analysis on these samples was carried out with the top 1000 variable genes based on VST. Uncertainty of hierarchical clustering on the DESeq2 datasets was assessed with pvclust (Suzuki and Shimodaira, 2006). For data shown in Figure S6H, the comparison of ZIKV and HSV datasets (each a separate experiment = batch) was performed by DESeq2 with batch correction (~batch+condition). Variance-stabilizing transformations (VSTs) were batch corrected by limma with the design (~batch+condition) (Ritchie et al., 2015) and analysis was performed on genes with abs(log2FC) > 1.

Quantification of apoptosis

To calculate the percentage of apoptotic cells, organoid cryosections immunostained with cleaved-caspase-3 (CC3) and DAPI were imaged under a confocal microscope. Random cortical structures on the surface of organoids were selected for quantification. The number of cells positive for CC3 in single z-plane images was counted manually using Fiji software. The total number of cells labeled by DAPI was estimated using the Fiji Plug-In GranFilter (using radius value set to 3 and step value set to 2) and watershed filter. The percentage of apoptosis is represented by the number of CC3+ cells divided by the total cell number labeled by DAPI.

Quantification of Sox1 levels

Organoid cryo-sections immunostained with Sox1 were imaged under a confocal microscope. Entire organoid sections were acquired using the "tile" and "stitching" functions in the Zen software (Zeiss). Single z-plane 8-bit images were used for quantification. Intensity (as mean gray value) of Sox1+ nuclei was measured using Fiji.

Quantification of IFN > GFP and ISRE > tdTomato positive cells

Organoid cryo-sections were immunostained with GFP and tdTomato antibodies and imaged under a confocal microscope using the "tile" and "stitching" functions in the Zen software (Zeiss). The total number of cells labeled by DAPI was estimated using the Fiji Plug-In GranFilter (using radius value set to 3 and step value set to 2) and watershed filter. Cells with high GFP signal were manually scored as IFN > GFP positive. Intensity (as mean gray value) of tdTomato signals was measured using Fiji and cells with tdTomato signal higher than the background intensity were scored as positive. Cells were scored to be within or outside the communication domain (200 μm in size) of a given IFN > GFP+ cell, a domain size compatible with paracrine signaling (Francis and Palsson, 1997).

PCR on viral nucleic acids

Viral nucleic acids were isolated from viral stocks using Purelink Viral RNA/DNA Mini Kit. PCR primer sequences are provided in the KEY RESOURCES TABLE. PCR amplification for TK was performed with GoTaq polymerase using the following program: 40 cycles of 30 s at 95°C, 30 s at 60°C, 1 min and 30 s at 72°C, with an additional incubation of 5 min at 72°C. Due to the high GC content of the ICP34.5 target sequence and the failure of amplification by GoTaq polymerase-based approaches, PCR amplification of ICP34.5 was performed with KOD Xtreme Hot Start DNA polymerase. The program consisted of 2 min at 94°C, followed by 30 cycles of 30 s at 98°C, 1 min at 60°C and 1 min at 68°C. PCR reactions were resolved on 1.25% agarose gels.

QUANTIFICATION AND STATISTICAL ANALYSIS

Statistical analysis was carried out with Prism software using unpaired t test for comparison of two groups and ANOVA for comparisons of multiple groups. For non-normal distributions, non-parametric tests were used. The threshold for statistical significance was $p < 0.05$. All details on sample size, the number of replicates, statistical tests and *p* values for each experiment are provided in the relevant figure, its legend or in Table S2. Unless differently specified in the figure legend, n refers to the number of replicates. Sample sizes of organoid experiments were estimated empirically based on previous experience. Organoids from the same batch were randomly allocated to different treatment groups during the first day of the experiment. Analyses were not performed blindly because of the substantial visual difference among groups.